INTERNATIONAL JOURNAL FOR NUMERICAL METHODS IN FLUIDS
Int. J. Numer. Meth. Fluids 0000; **00**:1–30
Published online in Wiley Online Library (www.onlinelibrary.wiley.com). DOI: 10.1002/fld.4696

High order ghost-point immersed boundary method for viscous compressible flows based on summation-by-parts operators

M. Ehsan Khalili[a,*], Martin Larsson[b], Bernhard Müller[a]

[a] *Department of Energy and Process Engineering, Norwegian University of Science and Technology (NTNU), Kolbjørn Hejes vei 2, NO-7491 Trondheim, Norway*
[b] *Sportradar AS, Ferjemannsveien 10, NO-7014 Trondheim, Norway*

SUMMARY

A high order immersed boundary method is devised for the compressible Navier–Stokes equations by employing high order summation-by-parts (SBP) difference operators. The immersed boundaries are treated as sharp interfaces by enforcing the solid wall boundary conditions via flow variables at ghost points. Two different interpolation schemes are tested to compute values at the ghost points and a hybrid treatment is used. The first method provides the bilinearly interpolated flow variables at the image points of the corresponding ghost points and the second method applies the boundary condition at the immersed boundary by using the weighted least squares method with high order polynomials. The approach is verified and validated for compressible flow past a circular cylinder at moderate Reynolds numbers. The tonal sound generated by vortex shedding from a circular cylinder is also investigated. In order to demonstrate the capability of the solver to handle complex geometries in practical cases, flow in a cross-section of a human upper airway is simulated.

Received . . .

KEY WORDS: High order finite difference method; Immersed boundary method; Compressible viscous flows

1. INTRODUCTION

Problems in many fields of science and engineering such as biomechanics often involve complex geometries and boundaries. Flow simulations for those problems require generating high quality body-conforming grids. This task becomes even more challenging when employing higher order methods. The accuracy of higher order numerical schemes is even more dependent on the quality of the computational grid. However, there are methods in computational fluid dynamics (CFD) dealing with complex boundaries which are based on Cartesian grids. The immersed boundary method (IBM) which has gained growing interest in recent decades and has demonstrated its usefulness for a wide range of applications. Even though this approach has appeared in various forms since its emergence, the primary concept of it is to take into account the effect of a solid body on the flow without changing the computational grid.

[*] Correspondence to: Corresponding author. Email: mohammadtaghi.khalili@ntnu.no, mt.e.khalili@gmail.com

The immersed boundary methods can generally be classified into two major groups, namely a continuous forcing approach and a discrete (or direct) forcing [1]. These methods can also be called diffuse and sharp interface methods, respectively [2]. In the first approach originated by Peskin [3, 4], a forcing term is added in the momentum equation and applied to the entire domain to enforce the boundary condition at the immersed boundary. Thus, a diffused boundary representing the effect of a solid body on the flow field is associated with the force distribution on the fluid. Many methods have been developed to determine the body force on the fluid. In the case of elastic boundaries, the boundary force can be determined by a distribution function on a particular segment at a time instant [3, 5]. If a rigid body is considered, a feedback forcing is added to satisfy the no-slip condition on the body surface, at which the force is dependent on the difference between the interpolated velocity at the boundary and the desired boundary condition [6, 7, 8]. This approach and its subsequent developments have been successfully used for a multitude of applications in incompressible fluid flow [9]. The significant advantage of continuous forcing approaches is that they are independent of the underlying spatial discretization. However, one of the drawbacks of these types of IBM are that they may not only induce spurious oscillations, but also numerical instability issues particularly for unsteady flows at high Reynolds numbers due to the inherent stiffness of the forcing terms [6, 10].

Conversely, in the discrete forcing approach, the governing equations are discretized on a Cartesian grid without computing any forcing term explicitly. In this approach, the presence of the solid surface imposed on the fluid is considered by adjusting the discretization in the vicinity of the immersed boundary in order to take the boundary conditions at the immersed boundary (IB) into account directly. Therefore, these sharp-interface approaches are better suited for higher accuracy than the diffuse-interface approaches. The sharp-interface methods have been developed in various formulations to deal with the fluid-solid interface.

In one type of the sharp-interface methods, the effect of the body is taken into account at the fluid nodal points in the vicinity of the fluid-solid interface. In this way, the presence of the body is incorporated into the reconstruction of the local flow field around the immersed interface. Thus, the flow field is locally reconstructed by employing a proper interpolation scheme satisfying the actual values of the boundary conditions. The approach was first proposed by Mohd–Yusof [11] for spectral methods. Fadlun et al. [12] further implemented the discrete-time forcing approach to a three-dimensional finite difference method on a standard marker-and-cell (MAC) staggered grid, as suggested by [11] and showed that this approach is more efficient than the continuous forcing one. A better reconstruction scheme of the fluid points near the immersed boundary was proposed by Balaras [13] who performed the reconstruction along the normal line to the body surface. Tseng and Ferziger [14] extended the concept of immersed boundary approaches proposed by Fadlun et al. [12] and Verzicco et al. [15] by means of a ghost cell approach originated in [16]. In their approach, a higher order representation of the IB is accomplished by employing ghost cells inside the solid body. Ghost cells are defined as cells within the solid body having at least one neighbouring cell inside the fluid domain. The concept behind this approach was to compute the flow variables at these ghost cells such that the boundary conditions at the IB are satisfied. Therefore, an interpolation scheme has to be formed for each ghost cell to implicitly incorporate the boundary condition at the immersed body surface. This approach is commonly referred as the ghost cell immersed boundary method (GCIBM). Ghias et al. [17] developed a finite difference-based ghost cell method for compressible viscous flows. The ghost cell immersed boundary method by Mittal et al. [18] has been proved to be able to deal with different problems, including highly complex geometries and moving or deforming bodies in sharp interface immersed boundary method.

The main difference between the works by Fadlun et al. [12], Balaras [13] and Gilmanov et al. [19] and the ghost cell immersed boundary methods in [18, 14, 17] is that the velocity field at the so-called forcing nodes (fluid points with at least one neighbouring point inside the solid body) is reconstructed by employing a linear interpolation scheme along either an arbitrary grid line [12] or a well-defined normal line [13, 19]. However, in the ghost cell IB by Mittal et al. [18] and Tseng and Ferziger [14], on the other hand, the solution is reconstructed at the ghost cells to present the geometric existence of the immersed boundary and to satisfy the discretization stencil. Both aforementioned strategies adopt the solid wall boundary conditions implicitly in their formulations.

Therefore, they can provide a sharp representation of the immersed boundary, which is necessary for high Reynolds numbers and compressible flows.

Moreover, there are several approaches employing the direct forcing method with diffuse interfaces [20, 21, 22]. In Uhlmann's approach [20], direct forcing is applied at Lagrangian markers on the body surface. The body forces are transferred to fluid points by using Peskin's regularized delta functions [5]. Similar combinations of direct and continuous forcing have been employed by Vanella and Balaras [21] and Wang and Zhang [22].

However, most of the attention on immersed boundary methods is devoted to incompressible flows [1]. Works on viscous compressible flows are still scarce and a few IB methods for viscous compressible flows and acoustic wave propagation problems have been developed [23]. Due to the different mathematical characteristic of the Navier–Stokes equations for compressible and incompressible flows, there are differences in the implementation of the boundary conditions between these two types of equations as well as in the spatial discretisation schemes employed [24, 25]. Furthermore, the vast majority of existing immersed boundary formulations particularly for viscous compressible flows are up to second order accuracy except for the studies by [23, 25]. The IBM employed by de Palma et al. [24] and de Tullio et al. [26] to deal with compressible turbulent flows over a circular cylinder and an airfoil is a direct forcing approach with a linear interpolation and inverse-distance weighted interpolation, respectively. Even though in the study by [26] local grid refinement is used, both of these methods lead to locally first order accurate approaches. In the compressible IB method of Ghias et al. [17], a finite difference based ghost cell method is developed using bilinear interpolation to determine the ghost cell values. Their method was successfully tested for flows over a circular cylinder and an airfoil at low Mach numbers showing second order accuracy locally and globally.

It is of great interest to develop a high order approach to expand the applications of the immersed boundary method [27] especially for compressible flows, in which in addition to boundary and shear layers generation and propagation of sound waves need to be resolved accurately and efficiently. In recent years, several efforts have been made to develop high order immersed boundary methods [23, 28, 29, 30, 31, 25]. The higher order ghost cell IBM for solving the linearized perturbed compressible equations for acoustic problems using a compact finite difference scheme was developed by Seo and Mittal [23]. Linnick and Fasel [31] presented a fourth order immersed boundary method based on a compact scheme for solving the incompressible Navier–Stokes equations in stream-function-vorticity formulation. High order correction terms for the jump conditions across the interface are introduced in their boundary treatment. That IBM was successfully applied to compressible flow by Brehm et al. [25]. The characteristic aspect of their new immersed boundary method [25] is that the coefficients of the irregular finite difference stencils in the vicinity of the immersed boundary are optimized to promote numerical stability. However, many additional studies of high order immersed boundary methods for the compressible Navier–Stokes equations are still lacking.

In the present study, an efficient high order method to solve viscous compressible flows with immersed boundaries is devised by combining a high order finite difference method based on summation-by-parts (SBP) operators and a high order immersed boundary method. We address how to implement IB methods for high order SBP operators on fixed Cartesian meshes. The SBP finite difference operator is chosen not only because it can accommodate a better resolution for small spatial scales with high accuracy, but also because of its inherent property due to the energy method to guarantee stability. In this study, a multi-dimensional ghost point methodology is employed to impose the boundary conditions at the immersed boundary. The method is devised for efficient and accurate solution of flows with arbitrary and complex boundaries. We exploit the methodologies of a second order ghost point method based on bilinear interpolation [18] and the weighted least-squares (WLSQ) method [32, 23] to devise a hybrid approach in order to obtain a high order accurate finite difference discretization for the compressible Navier–Stokes equations. Employing this combined strategy, we not only ensure the overall accuracy of the scheme but also physical values for all layers of ghost nodes. Before applying those methodologies to the compressible Navier–Stokes equations, we investigated the accuracy of the immersed boundary treatment for the steady heat equation with

Dirichlet and Neumann boundary conditions. Our high order IB method is verified and validated for compressible flow past a circular cylinder at Reynolds numbers 20, 40, 100 and 200. Flow-induced sound is also considered for investigating acoustic wave propagation at Mach numbers 0.1 and 0.2. Finally, we demonstrate the potential of the developed IB method to handle complex geometries by simulating viscous compressible airflow in the sagittal plane of the human upper airways of a specific patient.

The paper is organized as follows. In Section 2, the model for fluid flow is presented. In Section 3, the numerical method is described. There, the immersed boundary formulation is explained in detail, and the implementation of the boundary conditions is discussed. In section 4, results with our IBM are provided for steady heat conduction and for viscous compressible flow around a circular cylinder. The latter results are compared with numerical and experimental ones available in the literature. Then, the tonal sound generated by vortex shedding from a circular cylinder is investigated. Finally, the results for airflow in the sagittal plane of the human upper airways are presented. Conclusions are stated in Section 5.

2. COMPRESSIBLE NAVIER–STOKES EQUATIONS

In the present study, the 2D compressible Navier–Stokes equations in perturbation form are solved. The perturbation formulation is employed to minimize cancellation errors when discretizing the Navier–Stokes equations for compressible low Mach number flow [33, 34]. The conservative form of the 2D compressible Navier–Stokes equations in perturbation formulation can be written as

$$\mathbf{U}'_t + \mathbf{F}^{c\prime}_{x} + \mathbf{G}^{c\prime}_{y} = \mathbf{F}^{v\prime}_{x} + \mathbf{G}^{v\prime}_{y} \tag{1}$$

$\mathbf{U}' = \mathbf{U} - \mathbf{U_0}$ is the vector of conservative perturbation variables with $\mathbf{U} = (\rho, \rho u, \rho v, \rho E)^T$ the vector of the conservative variables and $\mathbf{U}_0 = (\rho_0, 0, 0, (\rho E)_0)^T$ the stagnation values.

The conservative perturbation variables $\mathbf{U}'$ and the inviscid $(\mathbf{F}^{c\prime}, \mathbf{G}^{c\prime})$ and viscous perturbation flux vectors $(\mathbf{F}^{v\prime}, \mathbf{G}^{v\prime})$ are defined by $\mathbf{F}^{c\prime} = \mathbf{F}^{c}(\mathbf{U}) - \mathbf{F}^{c}(\mathbf{U_0})$, etc, according to

$$\mathbf{U}' = \begin{pmatrix} \rho' \\ (\rho u)' \\ (\rho v)' \\ (\rho E)' \end{pmatrix}, \quad \mathbf{F}^{c\prime} = \begin{pmatrix} (\rho u)' \\ (\rho u)' u' + p' \\ (\rho v)' u' \\ ((\rho H)_0 + (\rho H)')u' \end{pmatrix}, \quad \mathbf{G}^{c\prime} = \begin{pmatrix} (\rho v)' \\ (\rho u)' v' \\ (\rho v)' v' + p' \\ ((\rho H)_0 + (\rho H)')v' \end{pmatrix},$$

$$\mathbf{F}^{v\prime} = \begin{pmatrix} 0 \\ \tau'_{xx} \\ \tau'_{xy} \\ u'\tau'_{xx} + v'\tau'_{xy} + \kappa T'_x \end{pmatrix}, \quad \mathbf{G}^{v\prime} = \begin{pmatrix} 0 \\ \tau'_{yx} \\ \tau'_{yy} \\ u'\tau'_{yx} + v'\tau'_{yy} + \kappa T'_y \end{pmatrix},$$

where t is the physical time and x and y are the Cartesian coordinates. ρ denotes density, u and v the x- and y-direction velocity components, E the specific total energy, T the temperature and κ the heat conduction coefficient calculated from the constant Prandtl number $\mathrm{Pr} = 0.72$. ρ_0, $(\rho E)_0$ and $(\rho H)_0$ denote the stagnation values of density, total energy density and total enthalpy density, respectively. The perturbation variables are given as follows

$$p' = p - p_0, \quad \rho' = \rho - \rho_0, \quad (\rho\mathbf{u})' = (\rho\mathbf{u}), \quad (\rho E)' = \rho E - (\rho E)_0, \quad (\rho H)' = (\rho E)' + p',$$
$$\mathbf{u}' = \frac{(\rho\mathbf{u})'}{\rho_0 + \rho'}, \quad \tau' = \mu(\nabla\mathbf{u}' + (\nabla\mathbf{u}')^T) - \tfrac{2}{3}\mu(\nabla\cdot\mathbf{u}')\mathbf{I}, \quad T' = \frac{p'/R - \rho' T_0}{\rho_0 + \rho'}.$$

Here, R is the specific gas constant and μ is the viscosity which is determined from the Sutherland law $\frac{\mu}{\mu_0} = (T/T_0)^{1.5}[(1 + S_c)/(T/T_0 + S_c)]$ with the non-dimensional Sutherland constant $S_c = 110\,\mathrm{K}/T_0$. Here, the stagnation temperature T_0 is used as the reference temperature.

Since perfect gas is considered, the pressure perturbation can be related to the conservative perturbation variables $p' = (\gamma - 1)[(\rho E)' - \frac{1}{2}((\rho\mathbf{u'}\cdot\mathbf{u}'))]$, where the ratio of specific heats $\gamma = c_p/c_v = 1.4$ for air.

The viscous flux vectors $\mathbf{F}^{v\prime}$ and $\mathbf{G}^{v\prime}$ are the same as for the standard conservative form, except for using the temperature perturbation T' instead of temperature T for the heat flux terms. The momentum density and velocity perturbations are taken as the same as their unperturbed counterparts, i.e. $(\rho\mathbf{u})' = \rho\mathbf{u}$ [35]. For convenience, the variables are non-dimensionalized with ρ_0, stagnation speed of sound c_0 and $\rho_0 c_0^2$ as reference values. In order to generalize the geometry for non-uniform Cartesian grids, the equations of motion are transformed from the physical domain (x, y) to the computational domain (ξ, η) by a mapping,

$$\begin{aligned} x &= x(\xi,\eta) \\ y &= y(\xi,\eta). \end{aligned} \tag{2}$$

Thus, the transformed 2D compressible Navier–Stokes equations in perturbation form are expressed as:

$$\hat{\mathbf{U}}'_t + \hat{\mathbf{F}}'_\xi + \hat{\mathbf{G}}'_\eta = 0 \tag{3}$$

where $\hat{\mathbf{U}}' = J^{-1}\mathbf{U}'$, $\hat{\mathbf{F}}' = J^{-1}(\xi_x(\mathbf{F}^{c\prime} - \mathbf{F}^{v\prime}) + \xi_y(\mathbf{G}^{c\prime} - \mathbf{G}^{v\prime}))$ and $\hat{\mathbf{G}}' = J^{-1}(\eta_x(\mathbf{F}^{c\prime} - \mathbf{F}^{v\prime}) + \eta_y(\mathbf{G}^{c\prime} - \mathbf{G}^{v\prime}))$. The chain rule for partial differentiation provides the expressions for Cartesian derivatives in the viscous flux vectors $\mathbf{F}^{v\prime}$ and $\mathbf{G}^{v\prime}$, e.g. $u'_x = u'_\xi\xi_x + u'_\eta\eta_x$ and $u'_y = u'_\xi\xi_y + u'_\eta\eta_y$. The Jacobian determinant of the transformation is $J^{-1} = x_\xi y_\eta - x_\eta y_\xi$ and metric terms are

$$\begin{aligned} J^{-1}\xi_x &= y_\eta, \quad J^{-1}\xi_y = -x_\eta, \\ J^{-1}\eta_x &= -y_\xi, \quad J^{-1}\eta_y = x_\xi. \end{aligned} \tag{4}$$

3. NUMERICAL METHOD

3.1. *Summation-by-parts (SBP) operators*

The high order finite difference method based on SBP operators [36, 37, 38] is employed for space discretization of the compressible Navier–Stokes equations. We use globally fourth order SBP operators to discretize the first ξ- and η- derivatives in (4) and (3). The SBP operators for $\frac{\partial}{\partial\xi}$ and $\frac{\partial}{\partial\eta}$ correspond to the sixth order central difference operator in the interior but degrade to third order accuracy near the boundaries, resulting in fourth order global accuracy [38]. This approach is based on the energy method, which permits to derive well-posedness for the continuous problem and to guarantee stability for the discrete problem. Summation-by-parts operators are discussed in [36, 37, 38]. The SBP operator Q used here is written as

$$Q = \frac{1}{h}\begin{pmatrix} q_{1,1} & q_{1,2} & q_{1,3} & q_{1,4} & q_{1,5} & q_{1,6} & 0 & \dots & & & & \\ q_{2,1} & q_{2,2} & q_{2,3} & q_{2,4} & q_{2,5} & q_{2,6} & 0 & \dots & & & & \\ q_{3,1} & q_{3,2} & q_{3,3} & q_{3,4} & q_{3,5} & q_{3,6} & 0 & \dots & & & & \\ q_{4,1} & q_{4,2} & q_{4,3} & q_{4,4} & q_{4,5} & q_{4,6} & q_{4,7} & 0 & \dots & & & \\ q_{5,1} & q_{5,2} & q_{5,3} & q_{5,4} & q_{5,5} & q_{5,6} & q_{5,7} & q_{5,8} & 0 & \dots & & \\ q_{6,1} & q_{6,2} & q_{6,3} & q_{6,4} & q_{6,5} & q_{6,6} & q_{6,7} & q_{6,8} & q_{6,9} & 0 & \dots & \\ & \dots & 0 & \frac{-1}{60} & \frac{3}{20} & \frac{-3}{4} & 0 & \frac{3}{4} & \frac{-3}{20} & \frac{1}{60} & 0 & \dots \\ & & & \ddots & \ddots & \ddots & \ddots & \ddots & \ddots & \ddots & \ddots & \ddots \end{pmatrix}, \tag{5}$$

where h is the grid spacing and $q_{i,j} \in \mathbb{R}, i = 1, \dots 6$ and $j = 1, \dots, 9$ are coefficients obtained by the order conditions and the SBP property [36, 38, 37]. The values of the coefficients derived by [36] are listed in Appendix A.

The second derivatives of the viscous parts of $\hat{\mathbf{F}_\xi}'$ and $\hat{\mathbf{G}_\eta}'$ are approximated by applying the first derivative SBP operator Q twice. However, successively applying the first derivative operator makes the stencil wider, which requires a special treatment for the immersed boundary method and will be discussed in section 3.3.1. Waves with wave number $k = \pi/h$, where h is the grid spacing, are not damped by viscous terms when applying the SBP operator Q twice because Q^2 in the interior does not damp waves with wave number $k = \pi/h$. Therefore, an explicit sixth order low pass filter is applied after each time step. The coefficient constant is chosen such that the waves with wave number $k = \pi/h$ is annihilated [34]. Studies by Visbal and Gaitonde [39] provide strong evidence that those waves can be successfully suppressed by applying higher order spatial filters. For the time integration process, the classical fourth order explicit Runge–Kutta method is used.

3.2. *Immersed boundary formulation*

The sharp interface method is well suited for compressible flow, because the boundary conditions at the immersed boundary are taken into account directly in this method, without computing any forcing term or introducing any force distribution function. In order to impose the boundary condition in a way that ensures a sharp interface separating the compressible fluid and the solid, a ghost point immersed boundary methodology is developed here.

The basic idea in this method is to compute the value of the flow variables at each of the ghost points (referring to the layer of points inside the solid body adjoining the immersed boundary) such that the boundary conditions at the immersed boundary are satisfied. As illustrated in Fig.1, the procedure begins by determining the immersed boundary and then identifying the solid points, i.e. the nodes lying inside the solid body, and the fluid points, i.e. the nodes lying outside the body in the fluid domain. Ghost points (denoted by GP) are points outside the computational domain which are included in a finite difference stencil centered around a fluid point. The image point (denoted by IP) can be found by extending a normal probe, i.e. a line normal to the immersed boundary, from the ghost point to intersect with the immersed boundary at the body intercept point (denoted by BI) such that the body intercept point lies at the midpoint of the line connecting the ghost point and the image point. Once the flow variables at the image point are computed, the ghost point variables can be determined by imposing the boundary conditions.

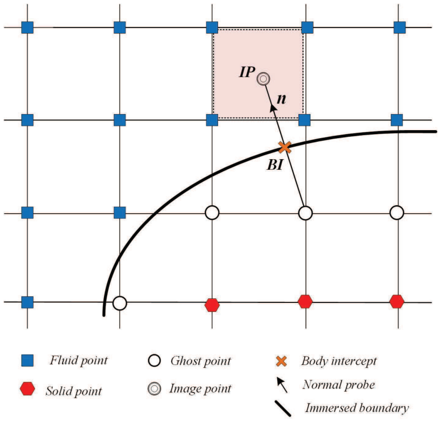

Figure 1. Schematic of points used to determine the flow variables at a ghost point adjacent to an immersed boundary.

An important aspect for employing this IBM is the evaluation of geometry information. The task of identifying, whether a grid node is a fluid point or a solid point is the classical problem of point-in-polygon for a 2D problem in computational geometry. Given a point in space and a polygon whose geometry is defined by its boundaries (edges), the question is whether the point is located inside or outside the polygon. The ray-casting algorithm is used in this study [40]. The ray-casting method works by casting a random half-infinite x-ray from a given point and counting the number of intersections between the ray and polygon edges. Once the intersections are identified it is straightforward to determine the grid point status. If the number of intersections is odd then the point is located inside the polygon (point B in Fig. 2(a)), otherwise it is located outside (point A in Fig. 2(a)).

In order to find the body intercept point and then the image point, the normal distance d from the ghost point to the surface of the geometry is obtained by a point-line distance algorithm. The surface of the geometry is discretized by body markers making up the surface segment. The normal vector $\mathbf{n}$ at the surface segment is calculated from the geometric coordinates of the points and the surface segment. Once the vector $\mathbf{r}$ between the ghost point and the closest body markers is identified, the normal distance is computed by projecting this vector onto the normal vector of the corresponding surface segment as illustrated in Fig. 2(b).

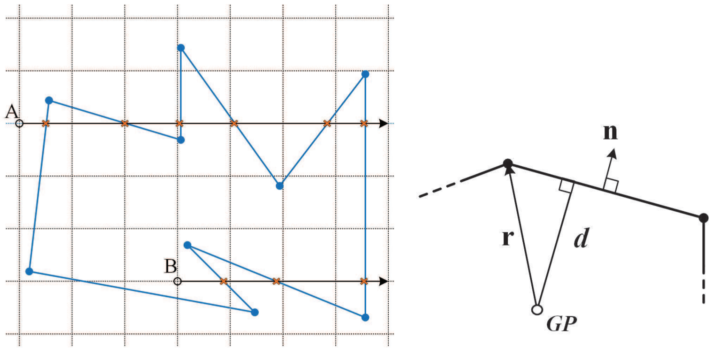

(a) (b)

Figure 2. (a) Schematic of ray-casting method for 2D point-in-polygon problem. (b) Schematic of point-normal line distance algorithm.

As mentioned in section 3.1, the high order SBP operators employed in this study for spatial discretization correspond to the sixth order central finite difference method at interior grid points. Thus, they require three layers of ghost points inside the immersed boundary in order to maintain the overall high order of accuracy, as shown in Fig. 3.

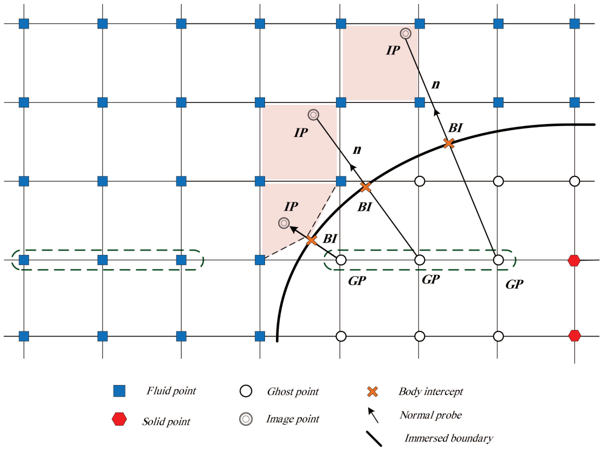

Figure 3. Schematic of 3 layers of ghost points inside immersed body on a Cartesian mesh.

A reconstruction procedure is needed to find the values at the ghost points by taking into account the boundary conditions directly. The reconstruction is built by a polynomial employing the nodal values in the fluid domain and the boundary conditions at the interface. In the present study, to preserve the globally high order accuracy of the SBP operator, two different ways of determining the values at the ghost points have been considered. Both approaches incorporate the boundary conditions at the body intercept.

Determining the ghost point values along the aforementioned normal probe by using image points for handling all layers of ghost points inside the solid body is one approach that we employed. However, it is constrained to second order accuracy [18, 41]. To achieve higher accuracy for the IBM, a high order polynomial interpolation combined with weighted least squares minimization [32, 23] is also used. Two kinds of interpolation methods are analyzed and discussed in detail later in this section, cf. 3.2.1 and 3.2.2, respectively. Finally, we have devised a hybrid approach to treat different layers of ghost points in order to obtain an efficient and high order boundary treatment. Even though our method is described here mostly within the context of a 2D problem, it can be readily extended to be applicable to 3D problems.

3.2.1. Bilinear interpolation Among the available options for determining the flow variables at the image points, the computationally most efficient way will be bilinear interpolation in 2D where the flow variables are bilinearly interpolated from the four nodal points surrounding the image point. The bilinear interpolation for a generic variable ϕ can be expressed as

$$\phi(x, y) = C_1 + C_2x + C_3y + C_4xy \tag{6}$$

The four unknown coefficients $C_i, i = 1, .., 4$, can be determined using values at the four nodes surrounding the image point. Thus, the variable at the image point is reconstructed through bilinear interpolation using unknown coefficients and known flow variables at surrounding fluid nodes. The four weighting coefficients are evaluated as the solution of the linear system

$$\mathbf{VC} = \phi, \tag{7}$$

where

$$\mathbf{C} = \{C_1, C_2, C_3, C_4\}^T \tag{8}$$

is the vector of the unknown coefficients and

$$\phi = \{\phi_1, \phi_2, \phi_3, \phi_4\}^T \tag{9}$$

is the vector of the four surrounding node values. The matrix $\mathbf{V}$ is the following Vandermonde matrix

$$\mathbf{V} = \begin{pmatrix} 1 & x_1 & y_1 & x_1y_1 \\ 1 & x_2 & y_2 & x_2y_2 \\ 1 & x_3 & y_3 & x_3y_3 \\ 1 & x_4 & y_4 & x_4y_4 \end{pmatrix}, \tag{10}$$

where $(x_i, y_i), i = 1, ..., 4$, are the Cartesian coordinates of the four surrounding nodes. In this classical formulation, the unknown coefficient values $C_i, i = 1, ..., 4$, would depend on the solution at each time step. However, the approach can be reformulated such that new coefficients are only dependent on the coordinates of the image point and the geometry of the grids [41]. Thus, the image point value can be expressed as

$$\phi_{\text{IP}} = \sum_{i=1}^{4} \alpha_i \phi_i, \tag{11}$$

where $\alpha_i, i = 1, ..., 4$, are coefficients depending on the coordinates only. The coefficients can be established once the grid, immersed boundary and image point coordinates are specified. When a ghost point is close to the immersed boundary, its corresponding image point might not have four surrounding fluid points. One case would be that the ghost point itself is part of the interpolation scheme. Since the ghost point value in an interpolation scheme would be unknown, the ghost point is then replaced by the body intercept point where the values are determined by the boundary conditions, cf. Fig.4(a).

For a Dirichlet boundary condition $\phi(x_{\rm BI}, y_{\rm BI}) = \phi_{\rm BI}$, the corresponding row in Eq. (10) is replaced by

$$\phi(x_{\rm BI}, y_{\rm BI}) = C_1 + C_2\, x_{\rm BI} + C_3\, y_{\rm BI} + C_4\, x_{\rm BI} y_{\rm BI} = \phi_{\rm BI}, \tag{12}$$

where $x_{\rm BI}$ and $y_{\rm BI}$ are the coordinates of the body intercept point. Thereby, for a Dirichlet boundary condition the linear system corresponding to Eq.(7) for this case becomes

$$\begin{pmatrix} 1 & x_1 & y_1 & x_1 y_1 \\ 1 & x_2 & y_2 & x_2 y_2 \\ 1 & x_3 & y_3 & x_3 y_3 \\ 1 & x_{\rm BI} & y_{\rm BI} & x_{\rm BI} y_{\rm BI} \end{pmatrix} \begin{pmatrix} C_1 \\ C_2 \\ C_3 \\ C_4 \end{pmatrix} = \begin{pmatrix} \phi_1 \\ \phi_2 \\ \phi_3 \\ \phi_{\rm BI} \end{pmatrix}. \tag{13}$$

For a Neumann boundary condition $\frac{\partial \phi(x_{\rm BI}, y_{\rm BI})}{\partial n} = \zeta$, the variable normal gradient at the body intercept is known instead of the actual value. The most obvious choice in such a case is to use the specified normal gradient value ζ to compute the value at the image point. The normal gradient of $\phi_{\rm BI}$ at the boundary can be determined by taking the normal derivative of Eq.(12),

$$\frac{\partial \phi(x_{\rm BI}, y_{\rm BI})}{\partial n} = C_2 n_x + C_3 n_y + C_4 (y_{\rm BI} n_x + x_{\rm BI} n_y) = \zeta, \tag{14}$$

where n_x and n_y are the components of the unit vector normal to the boundary.

Thus, the linear system corresponding to Eq.(7) for this case becomes

$$\begin{pmatrix} 1 & x_1 & y_1 & x_1 y_1 \\ 1 & x_2 & y_2 & x_2 y_2 \\ 1 & x_3 & y_3 & x_3 y_3 \\ 0 & n_x & n_y & y_{\rm BI} n_x + x_{\rm BI} n_y \end{pmatrix} \begin{pmatrix} C_1 \\ C_2 \\ C_3 \\ C_4 \end{pmatrix} = \begin{pmatrix} \phi_1 \\ \phi_2 \\ \phi_3 \\ \zeta \end{pmatrix} \tag{15}$$

As shown in Fig. 4(b), it can also occur that two interpolation points would lie inside the immersed body, one at the corresponding ghost point itself and one at another ghost point. The procedure we used to handle this case is to repeat the above steps for the other ghost point as well, resulting in a Vandermonde matrix where another row is also replaced by Eqs. (12) or (14) in the same way as the fourth row, in contrast to [18]. Applying our procedure for this case, it is no longer necessary to solve a coupled linear system by using iterative processes like [18]. This situation does not pose any consistency issues and ensures that the interpolation procedure for the image point is well-posed without affecting the accuracy of the interpolation.

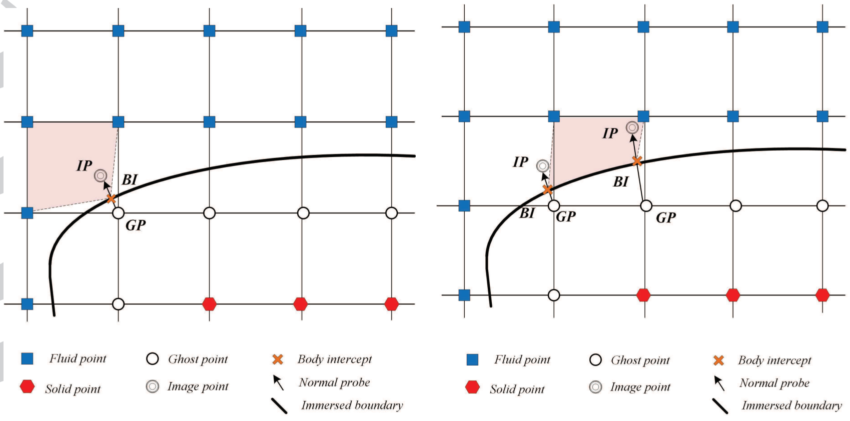

(a) (b)

Figure 4. (a) Schematic of the situation when one surrounding interpolation point is a body intercept. (b) Schematic of the situation when two of the surrounding interpolation points are body intercepts.

The value of the variable at the ghost point is computed by employing a linear approximation along the normal probe which takes into account the boundary condition at the body intercept. For a Dirichlet boundary condition this can generally be expressed as

$$\phi_{\text{BI}} = \tfrac{1}{2}(\phi_{\text{IP}} + \phi_{\text{GP}}) + \mathcal{O}(\triangle l^2) \tag{16}$$

where $\triangle l$ is the length of the normal probe from GP to IP. Solving for ϕ_{GP} using Eq. (16) and neglecting the truncation error gives

$$\phi_{\text{GP}} = \left(2 - \sum_{j \in \mathcal{G}} \alpha_j\right)\phi_{\text{BI}} - \sum_{i \notin \mathcal{G}} \alpha_i \phi_i \tag{17}$$

where $\mathcal{G}$ is the set of body intercepts that are part of the interpolation stencil. For a Neumann boundary condition at the immersed boundary $\frac{\partial\phi(x_{\text{BI}},y_{\text{BI}})}{\partial n} = (\frac{\partial\phi}{\partial n})_{\text{BI}}$, the following second order central difference approximation is applied along the normal probe

$$\left(\frac{\partial\phi}{\partial n}\right)_{\text{BI}} = \frac{\phi_{\text{IP}} - \phi_{\text{GP}}}{\triangle l} + \mathcal{O}(\triangle l^2) \tag{18}$$

Thereby to second order, the general formulation for a inhomogeneous Neumann boundary condition is expressed as

$$\phi_{\text{GP}} = \left(\sum_{j \in \mathcal{G}} \alpha_j - \triangle l\right)\left(\frac{\partial\phi}{\partial n}\right)_{\text{BI}} + \sum_{i \notin \mathcal{G}} \alpha_i \phi_i \tag{19}$$

3.2.2. Weighted least squares method To extend the boundary treatment to high order and to obtain more accurate values at the ghost points that are close to the immersed boundary, a high order polynomial interpolation combined with the weighted least squares method [32, 23] is used, here referred to as WLSQ method. In this approach, the value at the ghost point is determined by imposing the boundary condition at the body intercept point employing a third order polynomial to ensure at least fourth order accuracy of the flow reconstruction. In particular, a generic variable ϕ is approximated around the body intercept point $(x_{\text{BI}}, y_{\text{BI}})$ as follows

$$\phi(x', y') \approx \sum_{i=0}^{r}\sum_{j=0}^{r} C_{i,j}\, x'^{\,i}\, y'^{\,j}, \qquad i + j \leqslant r, \tag{20}$$

where r is the order of the polynomial, $x' = x - x_{\text{BI}}$ and $y' = y - y_{\text{BI}}$ are the local coordinates, and $C_{i,j}$ are the coefficients which link the boundary intercept point to neighbouring points. The number of polynomial coefficients to be determined is $p = f(r) = 10$ for a third order polynomial in the 2D case. Following [32, 23], the data points are chosen within a circular (spherical in 3D) region of radius R around the body intercept point, as shown in Fig. 5.

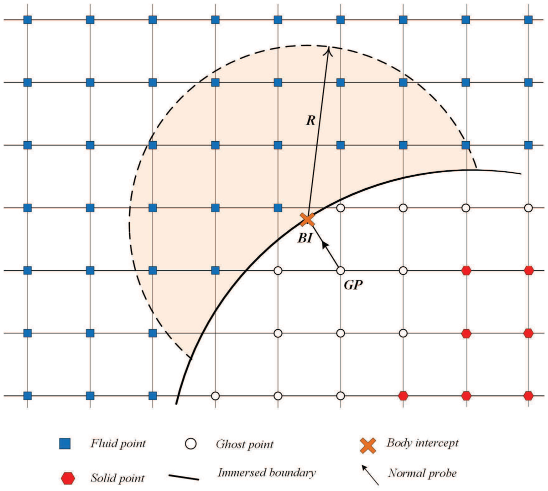

Figure 5. Schematic of polynomial approach for boundary treatment.

The unknown coefficients $\mathbf{C}$ can be determined by minimizing the weighted least squares error for q data points.

$$\min_{\mathbf{c}} \sum_{n=1}^{q} (w_n(\mathbf{V}_n\mathbf{C} - \phi_n))^2, \tag{21}$$

where n is the n^{th} data point, w_n is the exponential weighting function

$$w_n = e^{\frac{-d_n^2}{a_d}}, \qquad a_d = \sum_{n=1}^{q}(x_n'^{\,2} + y_n'^{\,2}) \tag{22}$$

where $d_n = \sqrt{(x'^{\,2} + y'^{\,2})} \leqslant R$ is the distance between the n^{th} data point and the body intercept point and a_d is a measure of data (fluid) points area which can be scaled to control the distribution of the weighting function. In Eq. 21, $\mathbf{C}$ can be read as

$$\mathbf{C} = \{C_{0,0}, C_{1,0}, C_{0,1}, ..., C_{r-1,0}, C_{0,r-1}, ..., C_{r-2,r-1}, C_{r-1,r-2}, C_{r,0}, C_{0,r}, \}^T. \tag{23}$$

$\mathbf{V}_n$ denotes row n of the Vandermonde matrix $\mathbf{V}$ where $\mathbf{V} = \{\mathbf{V}_1^T, \mathbf{V}_2^T, ..., \mathbf{V}_q^T\}^T$ and

$$\mathbf{V}_n = \{1, x^1y^0, x^0y^1, ..., x^{r-1}y^0, x^0y^{r-1}, ..., x^{r-2}y^{r-1}, x^{r-1}y^{r-2}, x^ry^0, x^0y^r\}. \tag{24}$$

Corresponding to the interpolating polynomial for third order in a 2D case, the Vandermonde matrix can be written following form

$$\mathbf{V} = \begin{pmatrix} 1 & x_1' & y_1' & \dots & x_1'^2 & y_1'^2 & \dots & x_1'^3 & y_1'^3 \\ \vdots & \vdots & \vdots & \vdots & \vdots & \vdots & \vdots & \vdots & \vdots \\ 1 & x_n' & y_n' & \dots & x_n'^2 & y_n'^2 & \dots & x_n'^3 & y_n'^3 \\ \vdots & \vdots & \vdots & \vdots & \vdots & \vdots & \vdots & \vdots & \vdots \\ 1 & x_q' & y_q' & \dots & x_q'^2 & y_q'^2 & \dots & x_q'^3 & y_q'^3 \end{pmatrix}. \tag{25}$$

The weighted least squares problem requires the number of data points to be larger than the number of unknown coefficients, i.e. $q > f(r)$. We found that the condition number of $\mathbf{V}$ gets very large, if the number of data points q is only sligthly larger than the number of polynomial coefficients $f(r)$. In previous studies [32, 23], the radial range R is adaptively chosen to get a well-conditioned matrix. However, in our study, we use a different algorithm to ensure that the matrix is always well-conditioned. In this algorithm, a sufficient amount of data points leading to a well-conditioned matrix is initially taken which is similar to [25] referred to as rank-based stencil selection. But, in contrast to [25], the minimum number of data points in the present study is not taken based on the rank-based stencil selection search. Having a fixed sufficiently large number of data points, the searching region is iteratively expanding to find all needed data points. The searching algorithm starts from an initially seeded data point which is a single fluid point closest to the body intercept.

Because the value at the ghost point in conjunction with the body intercept point needs to be found, the first row of the Vandermonde matrix is assigned to the ghost point coordinates $(x'_1, y'_1) = (x'_{\mathrm{GP}}, y'_{\mathrm{GP}})$ where $x'_{\mathrm{GP}} = x_{\mathrm{GP}} - x_{\mathrm{BI}}$ and $y'_{\mathrm{GP}} = y_{\mathrm{GP}} - y_{\mathrm{BI}}$. Thus, $q-1$ data points are found in the fluid domain. Nevertheless, because of using a ghost point outside the physical region of fluid domain in the WLSQ formulation, the approach requires the assumption that the solution of governing equations has a high order smooth extension outside its original domain. The coefficients $C_{i,j}$ which are the solution of the weighted least squares problem in Eq. 21 are given by

$$\mathbf{C} = (\mathbf{WV})^{+}\mathbf{W}\phi, \tag{26}$$

where the superscript $+$ indicates the pseudo–inverse of a matrix. $\mathbf{C}$ and ϕ are the coefficients and the data variables $\phi_n(x', y')$, respectively. $\mathbf{V}$ is the Vandermonde matrix and $\mathbf{W}$ is the weighting matrix given by

$$\mathbf{W} = \begin{pmatrix} w_1 & & & \\ & w_2 & & \\ & & \ddots & \\ & & & w_q \end{pmatrix}. \tag{27}$$

As mentioned earlier, the first row of $\mathbf{V}$ is assigned to the corresponding ghost point coordinates. Note that $(\mathbf{WV})$ is a $q \times p$ matrix where q is the number of data points and p is the number of coefficients. The pseudo-inverse of matrix $(\mathbf{WV})$ is computed by singular value decomposition (SVD) [42]. For the stationary body, once the grid geometry and the coordinates of the ghost and body intercept points are specified the pseudo-inverse of the $(\mathbf{WV})$ is computed and stored. Multiplication by the weighting matrix gives $\mathbf{M} = (\mathbf{WV})^{+}\mathbf{W}$ which is a $p \times q$ matrix. Since Eq. 20 is the approximation of $\phi(x', y')$ employing the Taylor series expansion from the body intercept point [23], the coefficients can be written as a linear combination of $\phi(x', y')$. For every ghost point associated with the body intercept point, the values and derivatives at the body intercept point can be represented by solving the weighted least squares error problem

$$C_{0,0} = \phi(x_{\mathrm{BI}}, y_{\mathrm{BI}}), \quad C_{1,0} = \frac{\partial \phi}{\partial x}, \quad C_{0,1} = \frac{\partial \phi}{\partial y}, \quad \ldots \tag{28}$$

Therefore, for a given Dirichlet boundary condition at the body, $\phi(x_{\mathrm{BI}}, y_{\mathrm{BI}}) = \phi_{\mathrm{BI}}$, the ghost point value can be evaluated as

$$\phi_{\mathrm{GP}} = \frac{\phi_{\mathrm{BI}} - \sum_{n=2}^{q} M(1,n) \cdot \phi(x'_n, y'_n)}{M(1,1)}. \tag{29}$$

For a given Neumann boundary condition at the body, $\frac{\partial \phi}{\partial n}(x_{\mathrm{BI}}, y_{\mathrm{BI}}) = \zeta$, the ghost point value is computed as

$$\phi_{\mathrm{GP}} = \frac{\zeta - \sum_{n=2}^{q} \Big(n_x M(2,n) + n_y M(3,n) \Big) \cdot \phi(x'_n, y'_n)}{n_x M(2,1) + n_y M(3,1)}, \tag{30}$$

where n_x and n_y are the components of the unit vector normal to the boundary. The WLSQ method has some similarities to the method by Seo and Mittal [23]. However, a different weighting function, cf. Eq. (22), is employed in the present work which we have found to be a robust choice for the weighting factors of data points. Furthermore, for the current WLSQ, the searching for data points is based on a fixed number of data points such that the Vandermonde matrix $\mathbf{V}$, cf. Eq. (25), is always well-conditioned.

3.2.3. Hybrid approach Despite the advantage of the WLSQ obtaining high order accuracy, it has to be noted that because in this approach the ghost point in conjunction with body intercept point is part of the interpolation formulation and it is located outside the domain, it is required to keep the ghost point close to the body intercept point by using fine grids. Furthermore, care has to be taken to have sufficient number of data points to ensure that the WLSQ problem is well-conditioned. On the other hand, by using the image point and bilinear interpolation a second order accurate solution will be achieved. For image points located too close to the immersed boundary, i.e., where one or two ghost points might be part of the interpolation scheme as discussed in section 3.2.1, the body intercept points need to be used instead which leads to losing a bit of weighting coefficients in the interpolation scheme. Therefore, to take advantage of the good features of these two approaches and make it compatible to our solver, we propose a hybrid treatment. In this approach, each layer of ghost points is treated differently. The first layer of ghost points is treated by using a third-order polynomial combined with the WLSQ in order to obtain a higher accuracy near the IB. The second and third layers of ghost points are treated by finding the image points of the corresponding ghost points and using bilinear interpolation to find the values at the image points as illustrated in Fig. 6.

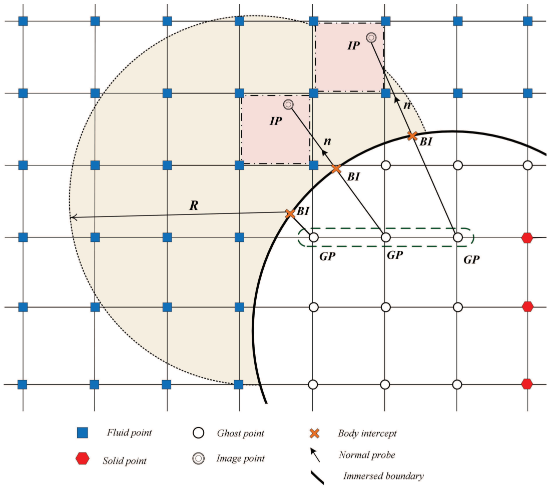

Figure 6. Schematic of hybrid treatment, WLSQ method is used for the first layer of ghost point and bilinear interpolation for the second and third layers.

Handling this treatment with a relatively large stencil may raise some concerns about obtaining non-physical values for the ghost points lying deep inside the solid body, i.e., far from the immersed boundary, at high Reynolds numbers. To avoid this situation and to maintain the accuracy, an improved high order interpolation polynomial combined with weighted least squares can be used for finding the values at the image points instead of bilinear interpolation. In this approach, the least squares method should be reformulated for data points around the image points rather than the body intercept points $x' = x - x_{\mathrm{IP}}$ and $y' = y - y_{\mathrm{IP}}$, as shown in Fig. 7. Since the value at the image point in conjunction with the body intercept point is required to be found, the first row of the Vandermonde matrix is assigned to the body intercept point instead, that is $(x'_1, y'_1) = (x'_{\mathrm{BI}}, y'_{\mathrm{BI}})$ where $x'_{\mathrm{BI}} = x_{\mathrm{BI}} - x_{\mathrm{IP}}$ and $y'_{\mathrm{BI}} = y_{\mathrm{BI}} - y_{\mathrm{IP}}$.

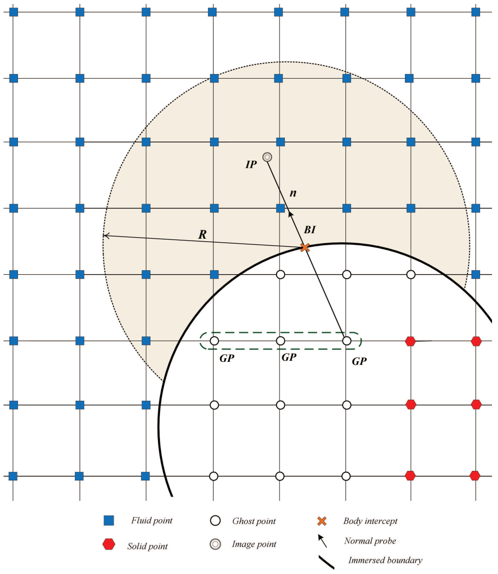

Figure 7. Schematic of polynomial approach for the third layer of ghost points to compute the value at the image point.

For a Dirichlet boundary condition $\phi(x_{BI}, y_{BI}) = \phi_{BI}$ at the immersed boundary, the Vandermonde matrix Eq. (25) is recast to

$$\mathbf{V} = \begin{pmatrix} 1 & x'_{\mathrm{BI}} & y'_{\mathrm{BI}} & x'_{\mathrm{BI}}y'_{\mathrm{BI}} & x'^2_{\mathrm{BI}} & \dots & y'^3_{\mathrm{BI}} \\ \vdots & \vdots & \vdots & \vdots & \vdots & \vdots & \vdots \\ 1 & x'_n & y'_n & x'_n y'_n & x'^2_n & \dots & y'^3_n \\ \vdots & \vdots & \vdots & \vdots & \vdots & \vdots & \vdots \\ 1 & x'_q & y'_q & x'_q y'_q & x'^2_q & \dots & y'^3_q \end{pmatrix} \tag{31}$$

For a Neumann boundary condition $\frac{\partial \phi(x_{\mathrm{BI}}, y_{\mathrm{BI}})}{\partial n} = \zeta$, specified at the body intercept point, the Vandermonde matrix Eq. (25) will have the following form

$$\mathbf{V} = \begin{pmatrix} 0 & n_x & n_y & x'_{\mathrm{BI}}n_y + y'_{\mathrm{BI}}n_x & 2x'^2_{\mathrm{BI}}n_x & \dots & 3y'^2_{\mathrm{BI}}n_y \\ \vdots & \vdots & \vdots & \vdots & \vdots & \vdots & \vdots \\ 1 & x'_n & y'_n & x'_n y'_n & x'^2_n & \dots & y'^3_n \\ \vdots & \vdots & \vdots & \vdots & \vdots & \vdots & \vdots \\ 1 & x'_q & y'_q & x'_q y'_q & x'^2_q & \dots & y'^3_q \end{pmatrix} \tag{32}$$

where n_x and n_y are the components of the unit vector normal to the boundary. Therefore, the value at the image point is computed from $\mathbf{M} = (\mathbf{WV})^{+}\mathbf{W}$ as

$$\phi_{\mathrm{IP}} = \sum_{n=1}^{q} M(1, n) \cdot \phi(x'_n, y'_n) \tag{33}$$

The gradient value at the image point can also be evaluated by the same analogy

$$\phi_{\mathrm{IP}} = \sum_{n=1}^{q} \Big(n_x M(2, n) + n_y M(3, n) \Big) \cdot \phi(x'_n, y'_n) \tag{34}$$

Generally, for small Reynolds numbers complete bilinear interpolations in the construction of image point values is used to treat the second and third layer of ghost points and for those are higher a high order polynomial interpolation combined with WLSQ can be used. Although having a high order accurate operator with relatively large stencil might sometimes cause lack of flexibility for the ghost point immersed boundary approach, it is unavoidable where the accuracy and grid resolution for problems are needed.

3.3. Boundary conditions

3.3.1. Immersed boundaries The no-slip boundary condition at the immersed boundary for a stationary body is considered. Thereby, Dirichlet boundary conditions are employed for the velocity components at the IB. For each velocity component, the corresponding value at the body intercept $\phi_{\mathrm{BI}} = 0$ is set in Eq. (12) and Eq.(29) for the bilinear interpolation and WLSQ, respectively. Applying the no-slip condition at the body surface, the convective flux contribution should be zero. The pressure gradient normal to the immersed interface is set to zero as a boundary layer approximation, $\frac{\partial p'}{\partial n} = \zeta = 0$ in Eqs. (14) and (30). Assuming an adiabatic boundary condition at the immersed body, the temperature gradient normal to the surface $\frac{\partial T'}{\partial n} = 0$ is set by enforcing a zero density gradient $\frac{\partial \rho'}{\partial n} = 0$. According to the boundary conditions considered for the immersed body, the values of the conservative perturbation variables at the ghost points are determined.

As mentioned above, applying the first derivative approximation twice for computing the second derivative will make the stencil wider. For the proper treatment of wide stencils in computing the second derivative, the first derivatives of the viscous fluxes are computed up to and including the ghost points in the third layer of ghost points as boundary points and using the globally fourth order SBP operator as discussed in section 3.1. The first derivatives of the viscous and inviscid fluxes, i.e. $\hat{F}'_\xi$ and $\hat{G}'_\eta$ are approximated by the standard sixth order central difference method. Using this procedure, we ensure that the derivatives of the inviscid and viscous fluxes at the fluid points closest to the immersed boundary are computed with high order.

3.3.2. Inflow and outflow boundaries Non-reflecting characteristic boundary conditions are employed at the inflow and outflow boundaries to minimize wave reflections. The Navier–Stokes characteristic boundary conditions (NSCBC) developed by [43] are employed to approximate incoming waves based on local one-dimensional inviscid (LODI) relations. The primitive variables can be related to the wave amplitude ($\mathscr{L}_i$) by LODI relations. The amplitudes of the characteristic waves are $\mathscr{L}_1 = \lambda_1(\frac{\partial p}{\partial x} - \rho c \frac{\partial u}{\partial x})$, $\mathscr{L}_2 = \lambda_2(c^2 \frac{\partial \rho}{\partial x} - \frac{\partial p}{\partial x})$, $\mathscr{L}_3 = \lambda_3(\frac{\partial v}{\partial x})$ and $\mathscr{L}_4 = \lambda_4(\frac{\partial p}{\partial x} + \rho c \frac{\partial u}{\partial x})$. Since fully non-reflecting conditions may lead to an ill-posed problem [43], this approach is partially reflecting. At the inflow a fixed velocity and temperature are imposed. The imposed velocity at the inlet requires the incoming wave amplitude to be equal to the outgoing wave $\mathscr{L}_4 = \mathscr{L}_1$. As the inlet temperature is fixed, an estimate of the entropy wave amplitude will be $\mathscr{L}_2 = \frac{1}{2}(\gamma - 1)(\mathscr{L}_1 + \mathscr{L}_4)$. The density ρ is computed at the inlet boundary from the continuity equation. Imposing a constant pressure at the outlet requires $\mathscr{L}_1 = -\mathscr{L}_4$. To keep the reflections low and the pressure close to atmospheric pressure, the incoming wave amplitude is set to

$$\mathscr{L}_1 = K(p - p_{\mathrm{atm}}) \tag{35}$$

where K is a relaxation coefficient. Rudy and Strikwerda proposed the relaxation coefficient as $K = \sigma(1 - \mathrm{Ma}^2)(c/L_t)$ where Ma is the Mach number, c the speed of sound, L_t the total length of the domain and σ a constant value [44]. The optimum value $\sigma = 0.25$ derived by [44] is employed. For reverse flow (negative velocity in x-direction) at the outlet, $\mathscr{L}_1$, $\mathscr{L}_2$ and $\mathscr{L}_3$ are set to zero.

4. RESULTS AND DISCUSSIONS

4.1. *Steady state heat equation*

To verify the order of spatial accuracy of two immersed boundary approaches mentioned above, a steady state heat transfer problem has been considered. Results from both bilinear interpolation and the WLSQ method are presented. The steady state heat equation reads

$$\nabla^2 T = \sigma \tag{36}$$

where σ is a source term, i.e. $-\kappa\sigma$ is the rate of heat generation per unit volume. The exact solution for this case in polar coordinates can be expressed as

$$T(r) = \sigma\,\frac{r^2}{4} + A\ln(r) + B \tag{37}$$

where A and B depend on the boundary conditions type and their values.

The numerical solution by means of IBM is implemented to solve Eq.(36) in Cartesian coordinates. The second and fourth order central finite difference methods for second derivatives are employed for spatial discretization of the regular fluid points:

$$D^{(2)}T_i = (T_{i+1} - 2T_i + T_{i-1})/\Delta x^2, \tag{38}$$

$$D^{(4)}T_i = (-T_{i+2} + 16T_{i+1} - 30T_i + 16T_{i-1} - T_{i-2})/(12\Delta x^2) \tag{39}$$

where the superscripts of the difference operators indicate their orders. The temperature distribution is solved between two concentrical cylinders with inner and outer diameters $D_{\text{inner}} = 3.5$ and $D_{\text{outer}} = 8.5$, respectively, embedded in a squares domain of edge length $L = 10$, cf. Fig. 8(a). The source term $\sigma = -0.45$ is chosen, and the temperatures of the inner and outer cylinders are $T_{\text{inner}} = 5$ and $T_{\text{outer}} = 10$, respectively. We also consider the cases, when one of the Dirichlet boundary conditions is replaced by the Neumann boundary condition $\frac{\partial T}{\partial n} = -0.5$. The immersed boundary approach is implemented at the cylinder interfaces.

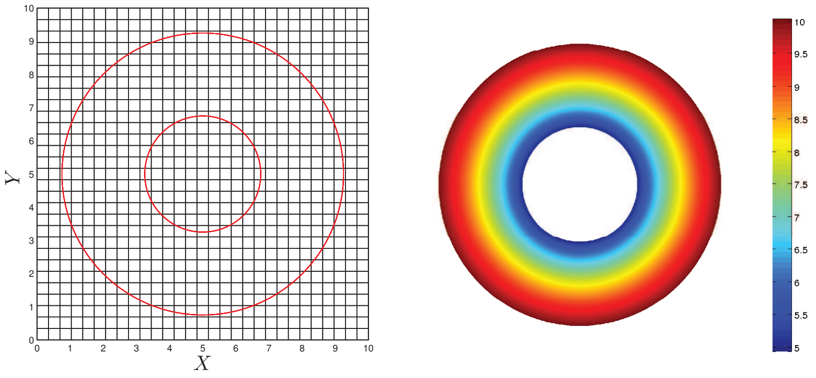

(a)

(b)

Figure 8. (a) The two concentrical cylinders immersed in a Cartesian grid. (b) Temperature contours of the heat equation, $N = 1000$.

The results from different grids on a uniform Cartesian grid ($N \times N$) from $N = 100$ to 1000 are compared with the exact solution to compute the L_2 and L_∞ norms. Fig. 8(b) shows temperature contours when Eq. (36) is solved by the IBM with $N = 1000$. The errors for different grids in three different cases of boundary conditions are presented in Fig. 9. To keep the discretization by fourth order central finite difference consistent, two layers of ghost points are considered. Once these two layers are treated by finding image points of corresponding ghost points and using bilinear interpolation and then by employing the fourth order weighted least squares method. A third order polynomial and $q = 17$ data points are used to keep the problem well-conditioned for WLSQ.

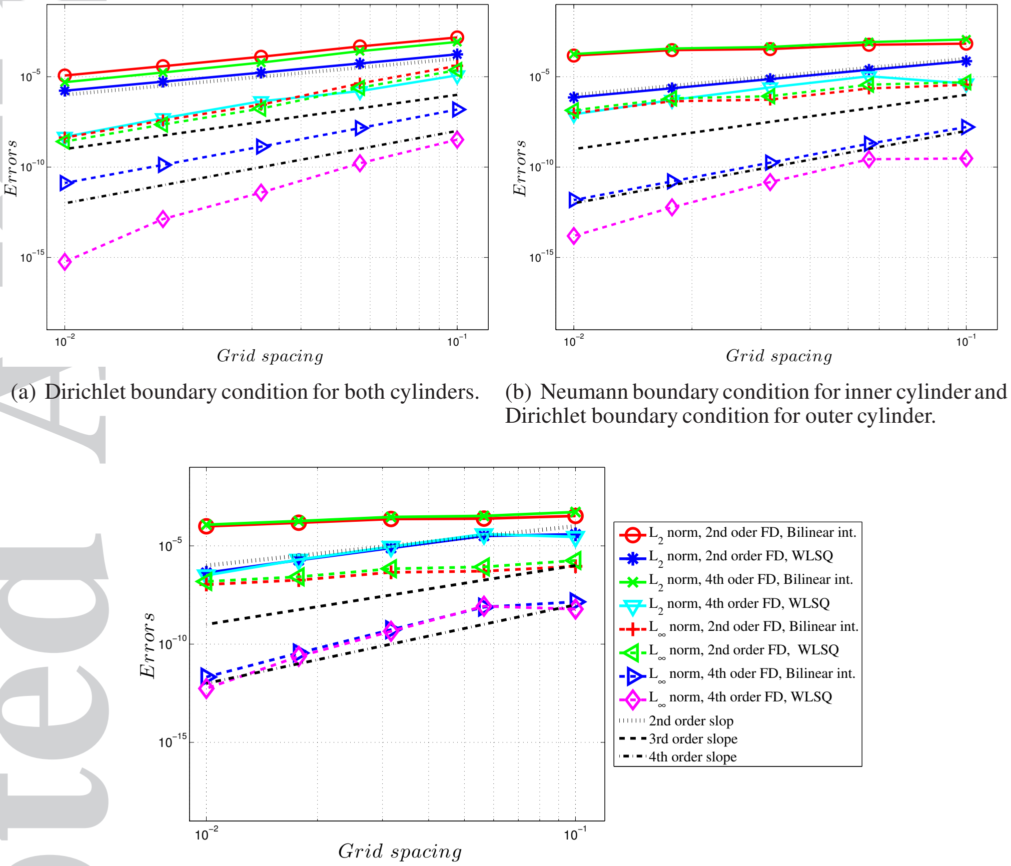

(a) Dirichlet boundary condition for both cylinders.

(b) Neumann boundary condition for inner cylinder and Dirichlet boundary condition for outer cylinder.

(c) Dirichlet boundary condition for inner cylinder and Neumann boundary condition for outer cylinder.

Figure 9. L_2 and L_∞ norms computed at various grid levels with IBM for 2D steady heat Eq.(36). The legend box is the same for all sub-figures.

The second, third and fourth order convergence rates are also included in Fig. 9 for reference. The results confirm that second order and third order convergence rates are obtained in the L_2 norm and third and fourth order accurate in the L_∞ norm of Dirichlet-Dirichlet boundary conditions, cf. 9(a) for the 2nd and 4th order centered difference methods using bilinear interpolation and WLSQ, respectively. For Dirichlet-Neumann boundary conditions, cf. Fig. 9(b) and 9(c), the L_2 norm of the 2nd and 4th order centered difference methods show second order and third order convergence rates, respectively. However, a non-monotone behavior appears when the grid is refined. Additionally, third and fourth order convergence is observed in the L_∞ norm.

4.2. *Flow past a circular cylinder*

4.2.1. Grid refinement study A convergence test for flow past a circular cylinder is carried out to assess the overall influence of the immersed boundary method on the high order scheme in our compressible flow solver. The Reynolds number $\mathrm{Re} = \frac{U_\infty D}{\nu} = 20$ and Mach numbers $\mathrm{Ma} = \frac{U_\infty}{c_\infty} = 0.03$ and $\mathrm{Ma} = 0.1$ are considered based on the free-stream velocity U_∞, the free-stream speed of sound c_∞, kinematic viscosity ν_∞ and cylinder diameter D. The overall fourth order SBP operators are combined with the hybrid IBM using the second order ghost point immersed boundary treatment for the second and third layers of ghost points and the high order weighted least squares method for the first layer of ghost points, cf. Section 3.2.3. For this test, a uniform Cartesian grid on a domain size of $7D \times 7D$ is used, where D is the cylinder diameter. The cylinder is placed at the point $(3.5D, 3.5D)$. For the immersed boundary formulation at the first layer of ghost points, the fourth order weighted least squares method based on a third-order polynomial is used. As mentioned above, a sufficient number of data points q should be taken such that the weighted least squares method is well-conditioned. Based on the condition number of the matrix $(\mathbf{WV})$, $q = 20$ is chosen. The same flow is computed on a series of grids with $175 \times 175, 350 \times 350, 700 \times 700, 1400 \times 1400$ grid points. Since the exact solution is not available, the results with a highly refined grid of 1400×1400 are used as a baseline. A time step of $\Delta t = 5 \times 10^{-4} D/c_0$ was chosen for the finest grid with $\Delta x = D/200$, and the CFL number is maintained the same for all grids, namely CFL = 0.1. The solution was integrated until $t = 40D/c_0$.

Symmetry boundary conditions are applied at the top and bottom of the computational domain. At the inflow, the velocities in the x- and y-directions are imposed using a uniform inlet profile normal to the boundary, $u(x = 0, t) = U_\infty$ and $v = 0$. In addition, the inlet temperature is set to $T = T_0 = 310$ K. The outlet pressure is set to atmospheric pressure, i.e., $p' = p - p_0 = p - p_{\text{atm}} = 0$ Pa. Navier–Stokes characteristic boundary conditions (NSCBC) [43] are applied at both the inlet and outlet in the streamwise direction, as mentioned in Section 3.3.2

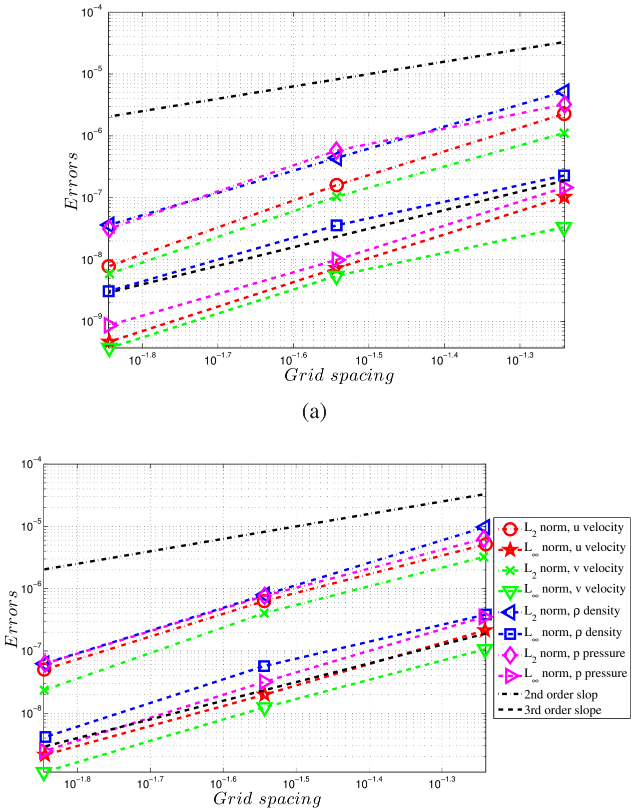

(a)

(b)

Figure 10. L_2 and L_∞ norms computed for velocity components, density and pressure at various grid levels for flow past over cylinder at Re=20 and (a) Ma = 0.03, (b) Ma = 0.1. The legend box is the same from both sub-figures.

The norms of the relative errors of the primitive variables ρ, u, v, p are indicators of accuracy of the fluid solver when the grid size changes. The velocity, density and pressure around the cylinder are used for comparing the results obtained by highly refined grids with those of the different resolutions. Figures 10(a) and 10(b) show the L_2 and L_∞ norms of the primitive flow variables for Ma = 0.03 and Ma = 0.1, respectively. The slopes of second and third accuracy are included in Fig.s 10(a) and 10(b) for reference. It is observed that third order convergence is achieved for the variables in the L_2 and L_∞ norms. The convergence results confirm that the current fluid flow solver with the hybrid treatment of immersed boundary is globally and locally third order accurate.

4.2.2. Verification and validation To verify and validate the present immersed boundary treatment for our compressible flow solver, the benchmark flow over a circular cylinder is first simulated at the Reynolds numbers $\mathrm{Re} = \frac{U_\infty D}{\nu}$ of 20 and 40 based on the free-stream velocity U_∞ kinematic viscosity ν_∞ and cylinder diameter D. It is known that steady flow over a circular cylinder can persist up to Reynolds numbers of about 47. The free-stream Mach number for the simulation is set as a small number $\mathrm{Ma} = \frac{U_\infty}{c_\infty} = 0.03$ in order to be comparable to the simulations performed using incompressible solvers. Then, unsteady flow over a circular cylinder has been chosen to verify and validate the proposed IB method at the Reynolds numbers of 100 and 200 and Mach number Ma = 0.25.

The computational domain size is $90D \times 40D$, where D is the diameter of the cylinder. The center of the cylinder is located at the point $(20D, 20D)$ of the coordinate system. The computational domain is sizeable to reduce the effects of the domain boundaries and wave reflections from the inlet and outlet boundaries. It has been observed that those wave reflections from the inlet and outlet boundaries could lead to a momentous error when computing the lift and drag coefficients. In the present work, a block structured computational domain has been discretized with non-uniform Cartesian grids (as shown in Fig.11(a)), where the block corresponding to the cylinder has a much finer grid spacing of $\Delta x = \Delta y = D/40$ at Re = 20 and 40, and grid spacing of $\Delta x = \Delta y = D/80$ at Re = 100 and 200. At these grid resolutions, the lift and drag coefficients are sufficiently converged. Sufficient grid resolution around the cylinder is crucial to obtain the drag and lift coefficients accurately. Additionally, to capture the von Kármán vortex street, the wake region needs to be resolved properly. The grid spacing Δx and Δy was smoothly stretched from $\Delta x = \Delta y = D/40$ at Re = 20 and 40, and $\Delta x = \Delta y = D/80$ for Re = 100 and Re = 200 to $\Delta x \approx \Delta y \approx D$ near the inflow, outflow, top and bottom boundaries. The hybrid IBM was employed, cf. Section 3.2.3. $q = 20$ and $q = 40$ fluid points surrounding the BI points are chosen for Re = 20 and 40 and Re = 100 and 200, respectively, for the formulation of the IB of the first layer of ghost points. The boundary conditions are exactly the same as in the previous Section 4.2.1.

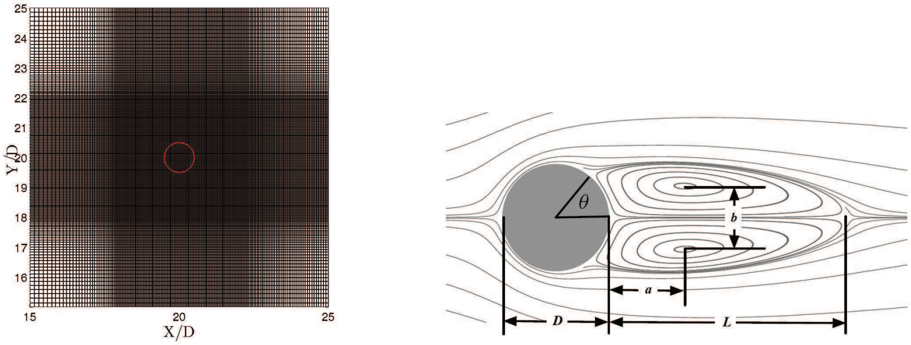

(a)

(b)

Figure 11. (a) Details of computational grid around circular cylinder. (b)Definitions of the relevant geometrical parameters of the symmetric separation region behind the cylinder [45].

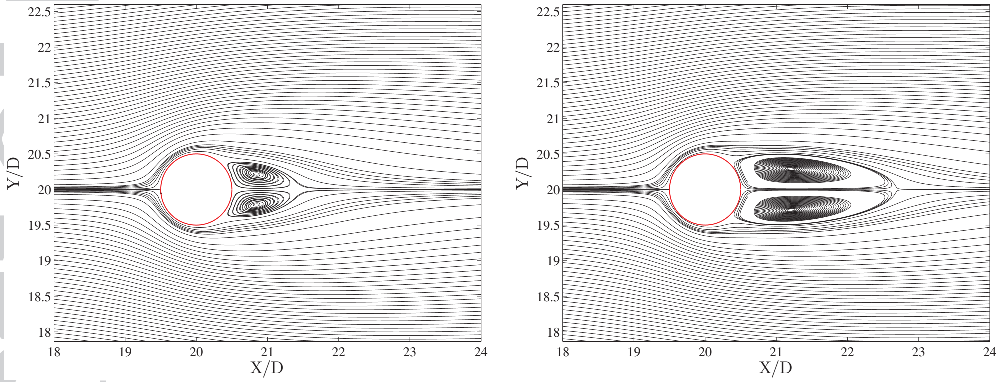

(a)

(b)

Figure 12. Streamlines for computed flow past a circular cylinder (a) Re = 20 and (b) Re = 40.

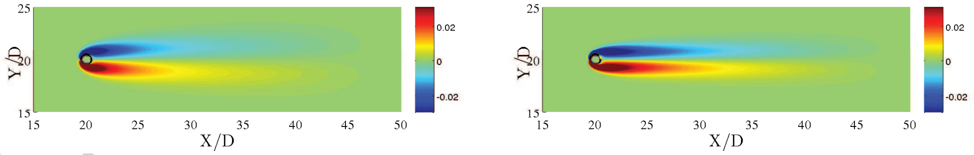

(a)

(b)

Figure 13. Vorticity contours for computed flow past a circular cylinder at Ma = 0.03 and (a) Re = 20 and (b) Re = 40.

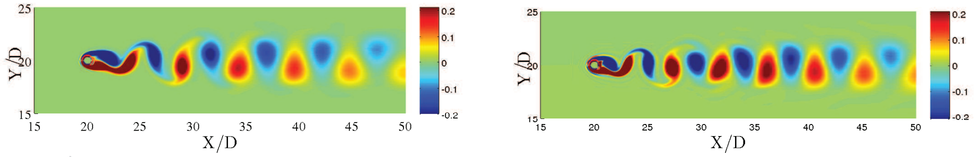

(a)

(b)

Figure 14. Spanwise vorticity contours for computed flow past a circular cylinder at Ma = 0.25 and (a) Re = 100 and (b) Re = 200.

The drag and lift coefficients are defined as $C_D = \frac{F_D}{\frac{1}{2}\rho_\infty U_\infty^2 D}$ and $C_L = \frac{F_L}{\frac{1}{2}\rho_\infty U_\infty^2 D}$, respectively, where ρ_∞ and U_∞ are free-stream density and velocity, respectively. D denotes the diameter of the cylinder, F_D and F_L are the drag and lift forces. The total force on the cylinder is given by the sum of the pressure and viscous forces integrated over the cylinder surface $F = -\oint p_B \cdot \mathbf{n}\, ds + \oint \tau_B \cdot \mathbf{n}\, ds$ where $\mathbf{n}$ is the outer unit vector normal to the cylinder, and p_B and τ_B are pressure and the viscous stress tensor on the body surface, respectively. These quantities are based on the evaluation of surface pressure and viscous stress. In the current solver, four nodes surrounding a body-intercept point corresponding to the first layer of ghost points are identified and then a bilinear interpolation is used to estimate the pressure and viscous stress tensor at the body intercept. The viscous stress at the involved ghost points and fluid points are computed by using our high order SBP operator.

The steady flow simulation results are quantified by determining the length of the separation region, the location of the counter rotating vortices in the cylinder wake, and the flow separation point on the cylinder surface (as shown in Fig.11(b)). Figures 12 and 13 present streamlines and contours of the spanwise vorticity ω_z, for the steady flow cases at Re = 20 and 40. The length of separation region grows, when the Reynolds number increases. A comparison of the accumulated data obtained in the current simulation and published results in the literature is provided in Table 1. The present numerical results are in good agreement with the previously published results.

Snapshots of iso-contours of the spanwise vorticity ω_z for the larger Reynolds number Re = 100 and Re = 200 are shown Fig. 14. These cases indicate the presence of the von Kármán vortex street because of the strong shear layer instability. The vortex shedding leads to time-varying lift and drag forces until they reach a periodic oscillatory form. The Strouhal number $St = \frac{fD}{U_\infty}$, where f is the vortex sheding frequency, is computed from the temporal variation of the lift coefficient. Due to the unsteadiness of the flow, the comparison of the average values of the lift and drag coefficients as well as the amplitude of the sinusoidal variation in time of the lift and drag coefficients is important.

Table I. Comparison of computed data with available numerical and experimental data at Re = 20 and Re = 40. (Exp.) indicates the experimental results.

			Re = 20			
	Ma	L	a	b	$\theta(deg)$	C_D
Tritton tritton1959experiments(Exp.)	-	-	-	-	-	2.09
Dennis & Chang dennis1970numerical	0	0.94	-	-	43.7	2.05
Coutanceau & Bouard coutanceau1977experimental(Exp.)	-	0.93	0.33	0.46	45.0	-
Fornberg fornberg1980numerical	0	0.91	-	-	45.7	2.0
Linnick & Fasel linnick2003high	0	0.93	0.36	0.43	43.5	2.06
De Palma et al. de2006immersed	0.03	0.93	0.36	0.43	44.6	2.05
Canuto & Taira canuto2015two	0	0.92	0.36	0.42	43.7	2.07
Present study	**0.03**	**0.93**	**0.36**	**0.43**	**43.9**	**2.05**

			Re = 40			
	Ma	L	a	b	$\theta(deg)$	C_D
Tritton tritton1959experiments(Exp.)	-	-	-	-	-	1.59
Dennis & Chang dennis1970numerical	0	2.35	-	-	53.8	1.52
Coutanceau & Bouard coutanceau1977experimental(Exp.)	-	2.13	0.76	0.59	53.8	-
Fornberg fornberg1980numerical	0	2.24	-	-	55.6	1.50
Linnick & Fasel linnick2003high	0	2.28	0.72	0.60	53.6	1.52
De Palma et al. de2006immersed	0.03	2.28	0.72	0.60	53.8	1.55
Canuto & Taira canuto2015two	0	2.24	0.72	0.59	53.7	1.54
Present study	**0.03**	**2.22**	**0.72**	**0.59**	**53.1**	**1.52**

Table II. Comparison of computed data with available numerical and experimental data at Re = 100 and Re=200. (Exp.) indicates the experimental results.

	Re = 100			
	Ma	St	C_D	C_L
Berger & Wille berger1972periodic(Exp.)	0	0.16-0.17	-	-
Liu et al. liu1998preconditioned	0	0.165	1.35 ± 0.012	± 0.339
Linnick & Fasel linnick2003high	0	0.166	1.34 ± 0.009	± 0.333
Mittal et al. mittal2008versatile	0	-	1.35	-
Karagiozis et al. karagiozis2010low	0.25	0.168	1.336	± 0.319
Canuto & Taira canuto2015two	0.25	0.163	1.378	± 0.325
Present study	**0.25**	**0.166**	$\mathbf{1.31 \pm 0.011}$	$\mathbf{\pm 0.323}$

	Re = 200			
	Ma	St	C_D	C_L
Berger & Wille berger1972periodic(Exp.)	0	0.18-0.19	-	-
Liu et al. liu1998preconditioned	0	0.192	1.31 ± 0.0049	± 0.69
Linnick & Fasel linnick2003high	0	0.197	1.34 ± 0.044	± 0.69
Belov et al. belov1995new	0	0.193	1.19 ± 0.042	- ± 0.64
Rogers & Kwak belov1995new	0	0.185	1.23 ± 0.050	± 0.65
Brehm et al. brehm2015locally	0.15	0.192	1.3 ± 0.04	± 0.64
Present study	**0.25**	**0.191**	$\mathbf{1.29 \pm 0.042}$	$\mathbf{\pm 0.64}$

Since the contours of the spanwise vorticity do not reduce significantly in amplitude in the wake of the cylinder, it indicates that the wake is sufficiently resolved for the given flow conditions in these two cases. These observations suggest that the quality of the block-structured grid and numerical methods employed for the cylinder simulations are adequate for the current analysis. The results for the time-averaged lift and drag coefficients, the amplitude of their changes as well as the Strouhal number of the present study are compared to published results in Table 2. Table 1 and 2 confirm that for the present study all results compare very well with results reported in the literature.

A low Mach number flow past a circular cylinder is now studied to investigate the generation of tonal sound. Mach numbers $\mathrm{Ma} = 0.1$ and $\mathrm{Ma} = 0.2$ at Reynolds number $\mathrm{Re} = 150$ are considered. The computational domain size is $200D \times 200D$, $X \in [-100D : 100D]$ and $Y \in [-100D : 100D]$, where D is the cylinder diameter. The cylinder is placed at the point $(0D, 0D)$. The hybrid approach outlined in Section 3.2.3 is used for the immersed boundary formulation. Therefore, at the first layer of ghost points, a third-order polynomial with $q = 40$ data points surrounding the BI points is used. The computational domain is discretized by non-uniform stretched meshes of 512×512 grid points with a refinement region around the immersed body. The refined mesh near the cylinder is a uniform grid with the minimal local grid spacing of $\Delta x = \Delta y = D/50$. Non-reflecting characteristic boundary conditions (NSCBC) are used for all outer farfield boundaries. At the top and bottom boundaries, NSCBC at outflow boundaries outlined in Section 3.3.2 is employed.

The contours of the instantaneous fluctuation pressure $\tilde{p}' = p'(x, y, t) - \bar{p}'(x, y)$ non-dimensionalized by $\rho_0 c_0^2$ are shown in Fig. 15 to visualize the acoustic field. p' is the perturbation pressure around the stagnation pressure p_0 defined in Section 2. The mean perturbation pressure $\bar{p}'$ is defined as

$$\bar{p}' = \frac{1}{t_p} \int_{t_0}^{t_0 + t_p} p'(x, y, t) dt, \tag{40}$$

where t_0 is the time instant when periodic vortex shedding is established and t_p indicates the period length. As can be seen, the wavelength of the acoustic waves for $\mathrm{Ma} = 0.1$ in Fig. 15(a) are two times bigger than those for $\mathrm{Ma} = 0.2$ in Fig. 15(b). It can be explained as the Strouhal number at $\mathrm{Re} = 150$ is equal for $\mathrm{Ma} = 0.1$ and $\mathrm{Ma} = 0.2$ and the sound waves are generated by vortex shedding [34].

The non-dimensional instantaneous fluctuation pressure on the positive and negative y-axis, i.e. at $\theta = \frac{\pi}{2}$ and $\theta = \frac{3\pi}{4}$, respectively, in cylindrical coordinates, indicates the same analogy that the wave length of the acoustic waves propagating in the positive and negative y- direction is basically halved for $\mathrm{Ma} = 0.2$ compared to $\mathrm{Ma} = 0.1$. The amplitudes of the non-dimensional instantaneous fluctuation pressure $\tilde{p'}$ divided by $\mathrm{Ma}^{2.5}$ at $\theta = \frac{\pi}{2}$, i.e. in the positive y-direction, are shown in Fig. 17, compared with the results in [34] where this problem was solved by the same flow solver on an O-type body-fitted grid and also compared with the results presented in [55]. The amplitudes obtained in the present IBM study are in good agreement with the reference solution [55] and the body-fitted grid simulation [34], they follow the same trend as the previous studies, cf. 17. We noted that the reference curves from Fig. 14(b) of [55] are correctly plotted as straight lines essentially proportional to $r^{-1/2}$ in our logarithmic plots of Fig. 17, while they were erroneously plotted as stright lines in the linear plots of Fig. 8 in [34].

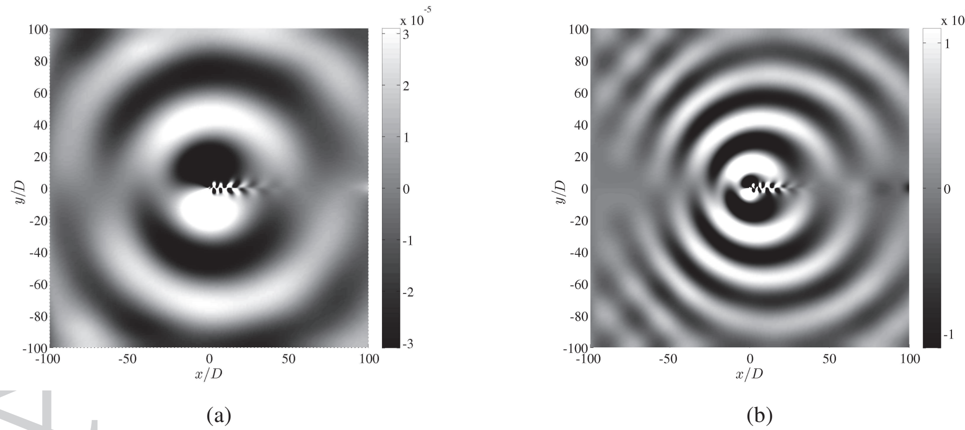

(a)

(b)

Figure 15. Non-dimensional instantaneous fluctuation pressure $\frac{\tilde{p}'}{\rho_\infty c_\infty^2}$ at $\mathrm{Re} = 150$ for (a) $\mathrm{Ma} = 0.1$ and (b) $\mathrm{Ma} = 0.2$.

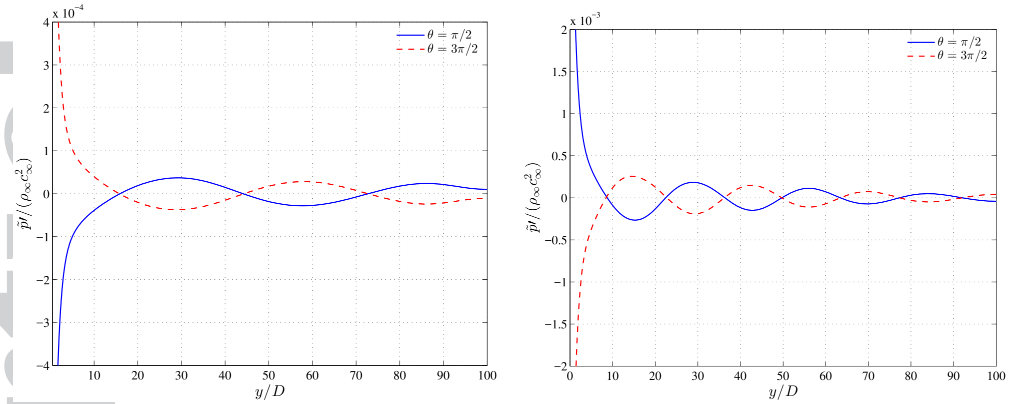

(a) (b)

Figure 16. Non-dimensional instantaneous fluctuation pressure $\frac{\tilde{p}'}{\rho_\infty c_\infty^2}$ at $\theta = \frac{\pi}{2}$ (solid line) and $\theta = \frac{3\pi}{2}$ (dashed line) for (a) $\mathrm{Ma} = 0.1$ and (b) $\mathrm{Ma} = 0.2$ at $\mathrm{Re} = 150$.

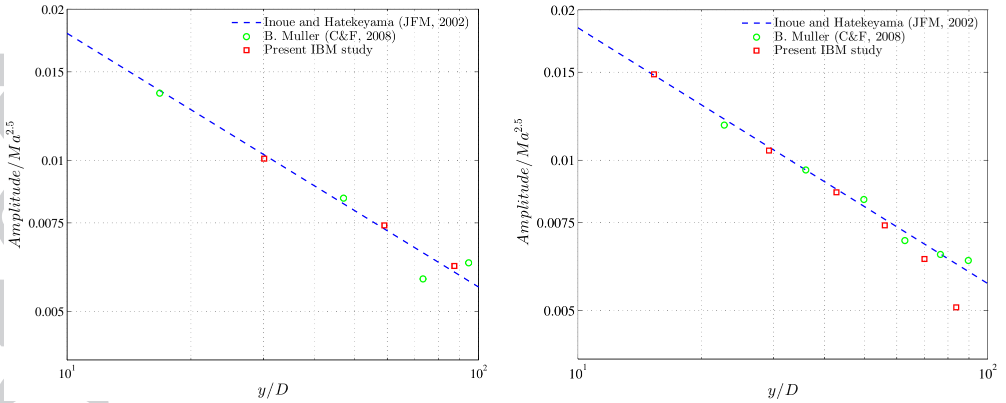

(a) (b)

Figure 17. Amplitude of scaled non-dimensional instantaneous fluctuation pressure $\frac{\tilde{p}'}{\rho_\infty c_\infty^2 \mathrm{Ma}^{2.5}}$ on positive y-axis for (a) $\mathrm{Ma} = 0.1$ and (b) $\mathrm{Ma} = 0.2$ at $\mathrm{Re} = 150$. Squares are the results of present study, circles are the results of [34] and dashed line [55].

4.3. Airflow in human upper airway

The present method is now applied to the real geometry of the human upper airway to demonstrate its capability for dealing with complex geometries in practical applications. Disorders of the upper airways are often associated with respiratory syndromes. Among those, obstructive sleep apnea (OSA) and snoring are closely related to the flow conditions in the upper airways. Obstructive sleep apnea syndrome (OSAS) is one of the most prevalent types of sleep-disorders caused by repetitive collapse of the soft tissues in the upper airways [56].

In the present study, a medical image, cf. Fig. 18(a), was provided by the Department of Radiology and Nuclear Medicine at St. Olavs Hospital, the university hospital in Trondheim, Norway. The computed tomography (CT) image is for patient number 12 in the study by [57], a 67-year-old man who showed great improvement in AHI (Apnea Hypopnea Index) after a septum plastic surgery in the nasal cavity such that he is no longer diagnosed with OSAS. In the present study, the cross-section of the upper airway from the nasopharynx to the laryngopharynx is considered for investigation as shown in Fig. 18(a) in dark green. As can be seen the tongue blocks the oral inlet. The geometry retrieval is provided by the Department of Structural Engineering at Norwegian University of Science and Technology (NTNU) [58]. The resulting 2D geometry in the sagittal plane is shown in Fig. 18(b). The airway pocket above the epiglottis was cut off during the geometry retrieval.

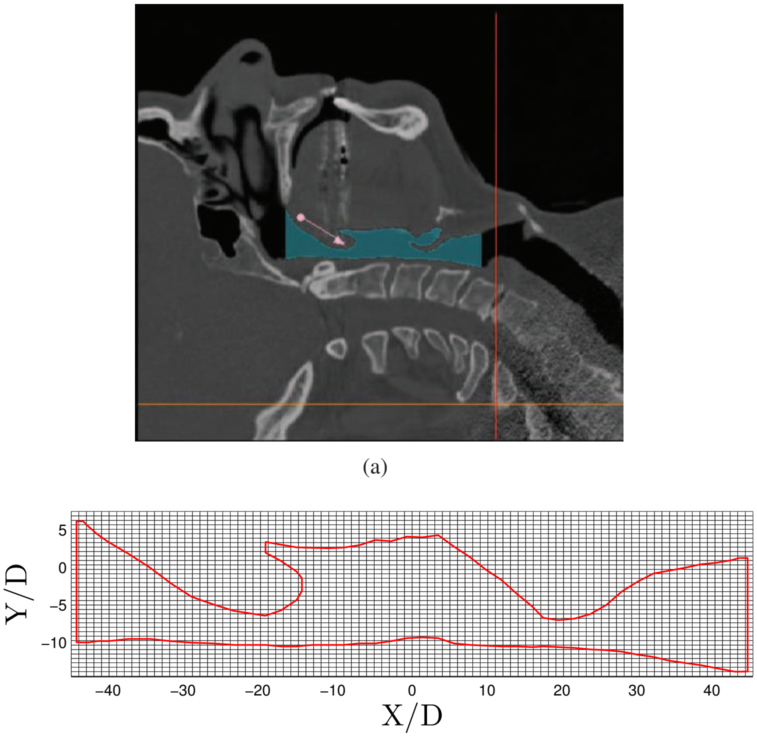

(a)

(b)

Figure 18. (a) CT image of the upper airway of a specific patient. Parts of the patient's head and neck are shown with nose and mouth near the top boundary. (b) Computational grid for upper airway simulation (every 10th grid point is plotted). The boundary of the flow domain is shown in red.

The computational grid for the upper airway geometry is shown in Fig. 18(b). The computational domain size is $90D \times 22D$, $X \in [-45D : 45D]$ and $Y \in [-14.5D : 7.5D]$, where D is the characteristic length scale for this case and is chosen as $D = 0.001$ m. A Cartesian grid with a total 991×381 grid points is employed, and the domain is resolved with grid spacings $\Delta x \approx 0.091D$ and $\Delta y \approx 0.058D$. A parabolic profile is employed for the inlet normal velocity distribution, and the maximum velocity is chosen as the velocity scale. A time step size $\triangle t$ corresponding to CFL = 0.35 is chosen to ensure stability.. The flow solver is integrated in time from the stagnant flow $\mathbf{U}' = 0$, except for the inlet velocity. All layers of ghost points to compute the flow field are treated by using bilinear interpolations to find the values at the image points. First, the simulation is carried out at Re = 70 based on the maximum inlet velocity $u_{max} = 3$ m/s, and Mach number is chosen as Ma = 0.03. Fig. 19 shows the spanwise vorticity ω_z at time instants $tc_0/D = 576$ and $tc_0/D = 960$. Pairs of vortices of opposite rotation are observed downstream of the first and the second constrictions formed by the soft palate and the epiglottis, respectively.

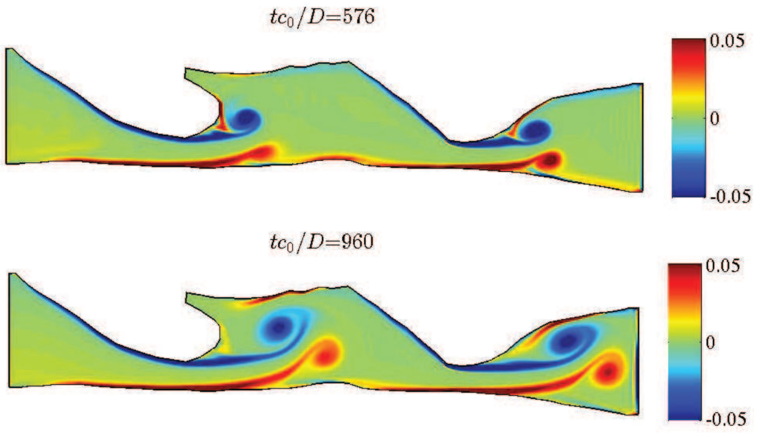

Figure 19. Time sequence showing vorticity contour plots for flow in the human upper airway at Re = 70 and Ma = 0.03.

Then, the simulation is repeated for Re = 2000 and the Ma = 0.1 based on the maximum inlet velocity $u_{max} = 33$ m/s. Fig. 20 presents a time sequence of vorticity contours. Complex vortical structures are observed and a large production of vorticity occurs in the oropharynx between soft palate and epiglottis and at the base of the epiglottis.

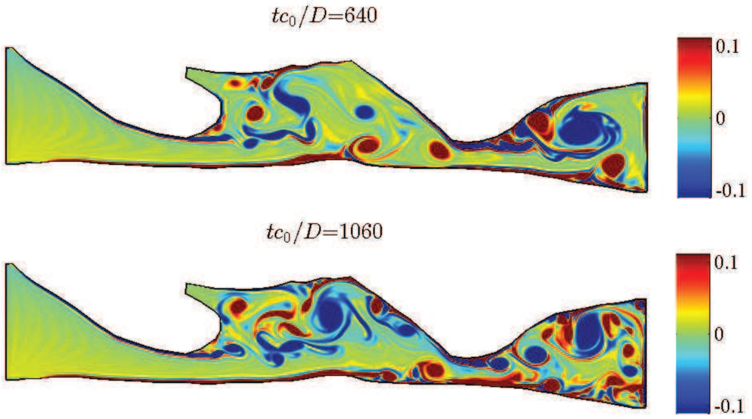

Figure 20. Time sequence showing vorticity contour plots for flow in the human upper airway at Re=2000 and Ma=0.1.

5. CONCLUSIONS

We have combined high order SBP operators with an immersed boundary method which permits to use Cartesian grids for arbitrary geometries for solving the compressible Navier–Stokes equations accurately and efficiently. The ghost point method is employed for the sharp representation of the immersed boundary. In the boundary condition treatment at the immersed boundary, both second order and high order methods are used. A hybrid method is applied to achieve an efficient and high order IBM formulation with SBP operators. The methodology is applied to compute steady and unsteady flow problems demonstrating its versatility as well as its accuracy. The flow past a circular cylinder for moderate values of Reynolds number and Mach number is assessed. The generation of tonal sound by uniform flow over a circular cylinder is investigated. Good agreement with available experimental and numerical results is achieved. The versatility of the present method is demonstrated by simulating flows in the human upper airway of an obstructive sleep apnea patient.

ACKNOWLEDGEMENTS

The present research is a part of a research project entitled ”Modeling of obstructive sleep apnea by fluid-structure interaction in the upper airways” funded by the Research Council of Norway under grant number 231741 [59]. The simulations in our work are done on the Vilje cluster at NTNU which is gratefully acknowledged. Finally, the authors thank Hongliang Liu and Bjørn Skallerud at the Department of Structural Engineering for providing the geometry retrieval of human upper airways.

A. COEFFICIENTS $q_{i,j}$ OF SBP OPERATOR Q

The free parameters in [36] is chosen such that the boundwith of Q is minimized, i.e. $q_{1,6} = 0$.

Table III. Coefficients $q_{i,j}$ of SBP operator Q strand1994summation.

$q_{1,1}$	-1.5825335189391164188	$q_{2,1}$	-0.4537473292821665418 0	$q_{3,1}$	-0.0024160826263371449650
$q_{1,2}$	1.9968007424231323418	$q_{2,2}$	0	$q_{3,2}$	-0.4522931267674904709 2
$q_{1,3}$	0.0047988863653014872884	$q_{2,3}$	0.20413995948833208469	$q_{3,3}$	0
$q_{1,4}$	-0.66986592424353432486	$q_{2,4}$	0.42505341435666916396	$q_{3,4}$	0.23791958686831427518
$q_{1,5}$	0.25079981439421691455	$q_{2,5}$	-0.19379006076750187297	$q_{3,5}$	0.34541374646501905816
$q_{1,6}$	0	$q_{2,6}$	0.018344016204667166126	$q_{3,6}$	-0.12862412393950571745
$q_{4,1}$	0.17061018846799776078	$q_{5,1}$	-0.086915492361728238331	$q_{6,1}$	0
$q_{4,2}$	-0.47641039995023947254	$q_{5,2}$	0.29554398882823409928	$q_{6,2}$	-0.025155437851495019140
$q_{4,3}$	-0.12035827579772345587	$q_{5,3}$	-0.23775972239854428505	$q_{6,3}$	0.079610054564964270222
$q_{4,4}$	0	$q_{5,4}$	-0.58114341331302103170	$q_{6,4}$	0.017590922581676217438
$q_{4,5}$	0.42710082726876904895	$q_{5,5}$	0	$q_{6,5}$	-0.68025083141176381057
$q_{4,6}$	-0.014377682403433476395	$q_{5,6}$	0.75652321103635055647	$q_{6,6}$	0
$q_{4,7}$	0.013435342414629595074	$q_{5,7}$	-0.16452964326520248826	$q_{6,7}$	0.73970913906075203762
$q_{4,8}$	0	$q_{5,8}$	0.018281071473911387584	$q_{6,8}$	-0.14794182781215040752
$q_{4,9}$	0	$q_{5,9}$	0	$q_{6,9}$	0.016437980868016711947

REFERENCES

REFERENCES

1. R. Mittal and G. Iaccarino, “Immersed boundary methods,” *Annu. Rev. Fluid Mech.*, vol. 37, pp. 239–261, 2005.
2. F. Sotiropoulos and X. Yang, “Immersed boundary methods for simulating fluid–structure interaction,” *Progress in Aerospace Sciences*, vol. 65, pp. 1–21, 2014.
3. C. S. Peskin, “Flow patterns around heart valves: a numerical method,” *Journal of Computational Physics*, vol. 10, no. 2, pp. 252–271, 1972.
4. C. S. Peskin, “Numerical analysis of blood flow in the heart,” *Journal of Computational Physics*, vol. 25, no. 3, pp. 220–252, 1977.
5. C. S. Peskin, “The immersed boundary method,” *Acta Numerica*, vol. 11, pp. 479–517, 2002.
6. D. Goldstein, R. Handler, and L. Sirovich, “Modeling a no-slip flow boundary with an external force field,” *Journal of Computational Physics*, vol. 105, no. 2, pp. 354–366, 1993.
7. E. Saiki and S. Biringen, “Numerical simulation of a cylinder in uniform flow: application of a virtual boundary method,” *Journal of Computational Physics*, vol. 123, no. 2, pp. 450–465, 1996.
8. M.-C. Lai and C. S. Peskin, “An immersed boundary method with formal second-order accuracy and reduced numerical viscosity,” *Journal of Computational Physics*, vol. 160, no. 2, pp. 705–719, 2000.
9. X. Yang, X. Zhang, Z. Li, and G.-W. He, “A smoothing technique for discrete delta functions with application to immersed boundary method in moving boundary simulations,” *Journal of Computational Physics*, vol. 228, no. 20, pp. 7821–7836, 2009.

10. D. Goldstein, R. Handler, and L. Sirovich, “Direct numerical simulation of turbulent flow over a modelled riblet-covered surface,” *Journal of Fluid Mechanics*, vol. 302, no. 10, pp. 333–376, 1995.
11. J. Mohd-Yusof, “Combined immersed-boundary/b-spline methods for simulations of flow in complex geometries.,” *Center for Turbulence Research Annual Research Briefs*, pp. 317 – 325, 1997.
12. E. Fadlun, R. Verzicco, P. Orlandi, and J. Mohd-Yusof, “Combined immersed-boundary finite-difference methods for three-dimensional complex flow simulations,” *Journal of Computational Physics*, vol. 161, no. 1, pp. 35–60, 2000.
13. E. Balaras, “Modeling complex boundaries using an external force field on fixed Cartesian grids in large-eddy simulations,” *Computers & Fluids*, vol. 33, no. 3, pp. 375–404, 2004.
14. Y.-H. Tseng and J. H. Ferziger, “A ghost-cell immersed boundary method for flow in complex geometry,” *Journal of Computational Physics*, vol. 192, no. 2, pp. 593–623, 2003.
15. R. Verzicco, M. Fatica, G. Iaccarino, and P. Orlandi, “Flow in an impeller-stirred tank using an immersed-boundary method,” *AIChE Journal*, vol. 50, no. 6, pp. 1109–1118, 2004.
16. S. Majumdar, G. Iaccarino, and P. Durbin, “RANS solvers with adaptive structured boundary non-conforming grids,” *Annual Research Briefs, Center for Turbulence Research, Stanford University*, pp. 353–466, 2001.
17. R. Ghias, R. Mittal, and H. Dong, “A sharp interface immersed boundary method for compressible viscous flows,” *Journal of Computational Physics*, vol. 225, no. 1, pp. 528–553, 2007.
18. R. Mittal, H. Dong, M. Bozkurttas, F. Najjar, A. Vargas, and A. von Loebbecke, “A versatile sharp interface immersed boundary method for incompressible flows with complex boundaries,” *Journal of Computational Physics*, vol. 227, no. 10, pp. 4825–4852, 2008.
19. A. Gilmanov, F. Sotiropoulos, and E. Balaras, “A general reconstruction algorithm for simulating flows with complex 3D immersed boundaries on cartesian grids,” *Journal of Computational Physics*, vol. 191, no. 2, pp. 660–669, 2003.
20. M. Uhlmann, “An immersed boundary method with direct forcing for the simulation of particulate flows,” *Journal of Computational Physics*, vol. 209, no. 2, pp. 448–476, 2005.
21. M. Vanella and E. Balaras, “Short note: A moving-least-squares reconstruction for embedded-boundary formulations,” *Journal of Computational Physics*, vol. 228, no. 18, pp. 6617–6628, 2009.
22. S. Wang and X. Zhang, “An immersed boundary method based on discrete stream function formulation for two-and three-dimensional incompressible flows,” *Journal of Computational Physics*, vol. 230, no. 9, pp. 3479–3499, 2011.
23. J. H. Seo and R. Mittal, “A high-order immersed boundary method for acoustic wave scattering and low-Mach number flow-induced sound in complex geometries,” *Journal of Computational Physics*, vol. 230, no. 4, pp. 1000–1019, 2011.
24. P. De Palma, M. De Tullio, G. Pascazio, and M. Napolitano, “An immersed-boundary method for compressible viscous flows,” *Computers & Fluids*, vol. 35, no. 7, pp. 693–702, 2006.
25. C. Brehm, C. Hader, and H. F. Fasel, “A locally stabilized immersed boundary method for the compressible Navier–Stokes equations,” *Journal of Computational Physics*, vol. 295, pp. 475–504, 2015.
26. M. D. de Tullio, P. De Palma, G. Iaccarino, G. Pascazio, and M. Napolitano, “An immersed boundary method for compressible flows using local grid refinement,” *Journal of Computational Physics*, vol. 225, no. 2, pp. 2098–2117, 2007.
27. C. Zhu, H. Luo, and G. Li, “High-order immersed-boundary method for incompressible flows,” *AIAA Journal*, pp. 2734–2741, 2016.
28. S. Laizet and E. Lamballais, “High-order compact schemes for incompressible flows: A simple and efficient method with quasi-spectral accuracy,” *Journal of Computational Physics*, vol. 228, no. 16, pp. 5989–6015, 2009.
29. Y. Zhou, S. Zhao, M. Feig, and G.-W. Wei, “High order matched interface and boundary method for elliptic equations with discontinuous coefficients and singular sources,” *Journal of Computational Physics*, vol. 213, no. 1, pp. 1–30, 2006.
30. F. Gibou and R. Fedkiw, “A fourth order accurate discretization for the laplace and heat equations on arbitrary domains, with applications to the Stefan problem,” *Journal of Computational Physics*, vol. 202, no. 2, pp. 577–601, 2005.
31. M. N. Linnick and H. F. Fasel, “A high-order immersed interface method for simulating unsteady incompressible flows on irregular domains,” *Journal of Computational Physics*, vol. 204, no. 1, pp. 157–192, 2005.
32. H. Luo, R. Mittal, X. Zheng, S. A. Bielamowicz, R. J. Walsh, and J. K. Hahn, “An immersed-boundary method for flow–structure interaction in biological systems with application to phonation,” *Journal of Computational Physics*, vol. 227, no. 22, pp. 9303–9332, 2008.
33. J. Sesterhenn, B. Müller, and H. Thomann, “On the cancellation problem in calculating compressible low Mach number flows,” *Journal of Computational Physics*, vol. 151, no. 2, pp. 597–615, 1999.
34. B. Müller, “High order numerical simulation of aeolian tones,” *Computers & Fluids*, vol. 37, no. 4, pp. 450–462, 2008.
35. M. Larsson and B. Müller, “Numerical simulation of confined pulsating jets in human phonation,” *Computers & Fluids*, vol. 38, no. 7, pp. 1375–1383, 2009.
36. B. Strand, “Summation by parts for finite difference approximations for d/dx,” *Journal of Computational Physics*, vol. 110, no. 1, pp. 47–67, 1994.
37. B. Gustafsson, H.-O. Kreiss, and J. Oliger, *Time dependent problems and difference methods*. John Wiley & Sons, New York, 1995.
38. B. Gustafsson, *High order difference methods for time dependent PDE*. Springer, Berlin, 2008.
39. M. R. Visbal and D. V. Gaitonde, “On the use of higher-order finite-difference schemes on curvilinear and deforming meshes,” *Journal of Computational Physics*, vol. 181, no. 1, pp. 155–185, 2002.
40. E. Haines, “Point in polygon strategies,” *Graphics gems IV*, vol. 994, pp. 24–26, 1994.
41. M. E. Khalili, M. Larsson, and B. Müller, “Immersed boundary method for the compressible Navier–Stokes equations using high order summation-by-parts difference operators,” in *Proceedings of the 12th International*

Conference on Computational Fluid Dynamics In the Oil & Gas, Metallurgical and Process Industries, pp. 233–242, SINTEF, May 30th - June 1st 2017.

42. W. H. Press, S. A. Teukolsky, W. T. Vetterling, and B. P. Flannery, "Numerical recipes: The art of scientific computing," *Third edition, Cambridge University Press, Cambridge*, 2007.
43. T. J. Poinsot and S. Lele, "Boundary conditions for direct simulations of compressible viscous flows," *Journal of Computational Physics*, vol. 101, no. 1, pp. 104–129, 1992.
44. D. H. Rudy and J. C. Strikwerda, "A nonreflecting outflow boundary condition for subsonic Navier-Stokes calculations," *Journal of Computational Physics*, vol. 36, no. 1, pp. 55–70, 1980.
45. D. Canuto and K. Taira, "Two-dimensional compressible viscous flow around a circular cylinder," *Journal of Fluid Mechanics*, vol. 785, pp. 349–371, 2015.
46. D. Tritton, "Experiments on the flow past a circular cylinder at low Reynolds numbers," *Journal of Fluid Mechanics*, vol. 6, no. 04, pp. 547–567, 1959.
47. S. Dennis and G.-Z. Chang, "Numerical solutions for steady flow past a circular cylinder at Reynolds numbers up to 100," *Journal of Fluid Mechanics*, vol. 42, no. 03, pp. 471–489, 1970.
48. M. Coutanceau and R. Bouard, "Experimental determination of the main features of the viscous flow in the wake of a circular cylinder in uniform translation. Part 1. Steady flow," *Journal of Fluid Mechanics*, vol. 79, no. 02, pp. 231–256, 1977.
49. B. Fornberg, "A numerical study of steady viscous flow past a circular cylinder," *Journal of Fluid Mechanics*, vol. 98, no. 04, pp. 819–855, 1980.
50. M. Linnick and H. Fasel, "A high-order immersed boundary method for unsteady incompressible flow calculations," in *41st Aerospace Sciences Meeting and Exhibit*, pp. 1124–1141, 2003.
51. E. Berger and R. Wille, "Periodic flow phenomena," *Annual Review of Fluid Mechanics*, vol. 4, no. 1, pp. 313–340, 1972.
52. C. Liu, X. Zheng, and C. Sung, "Preconditioned multigrid methods for unsteady incompressible flows," *Journal of Computational Physics*, vol. 139, no. 1, pp. 35–57, 1998.
53. K. Karagiozis, R. Kamakoti, and C. Pantano, "A low numerical dissipation immersed interface method for the compressible Navier–Stokes equations," *Journal of Computational physics*, vol. 229, no. 3, pp. 701–727, 2010.
54. A. Belov, L. Martinelli, and A. Jameson, "A new implicit algorithm with multigrid for unsteady incompressible flow calculations," in *33rd Aerospace sciences meeting and exhibit*, p. 49, 1995.
55. O. Inoue and N. Hatakeyama, "Sound generation by a two-dimensional circular cylinder in a uniform flow," *Journal of Fluid Mechanics*, vol. 471, pp. 285–314, 2002.
56. M. Khalili, M. Larsson, and B. Müller, "Interaction between a simplified soft palate and compressible viscous flow," *Journal of Fluids and Structures*, vol. 67, pp. 85–105, 2016.
57. M. H. S. Moxness and S. Nordgård, "An observational cohort study of the effects of septoplasty with or without inferior turbinate reduction in patients with obstructive sleep apnea," *BMC Ear, Nose and Throat Disorders*, vol. 14, no. 1, p. 11, 2014.
58. H. Liu and B. Skallerud, *Private communication*, 2017.
59. M. Larsson, *Welcome to the OSAS page*, 2015. http://osas.no/.